DEVELOPMENT OF IRON OXIDE BASED NANOPARTICLES AS DUAL-MODALITY IMAGING PROBES

APPROVED BY SUPERVISORY COMMITTEE

Xiankai Sun, Ph.D. (Mentor)

Orhan K. Öz, M.D., Ph.D.

Padmakar Kulkarni, Ph.D.

Liping Tang, Ph.D.

Peter P. Antich, Ph.D. (Chairman)

DEVELOPMENT OF IRON OXIDE BASED NANOPARTICLES AS DUAL-MODALITY IMAGING PROBES

By

YI GUO

THESIS

Presented to the Faculty of the Graduate School of Biomedical Sciences

The University of Texas Southwestern Medical Center at Dallas

In Partial Fulfillment of the Requirements

For the Degree of

MASTER OF SCIENCE

The University of Texas Southwestern Medical Center at Dallas

Dallas, Texas
August, 2008

This thesis is dedicated to my parents

ACKNOWLEDGEMENT

I acknowledge all the people who love me, support me and continuously encourage me throughout the journey of my life.

Most importantly, I would like to acknowledge Dr. Xiankai Sun for his invaluable guidance during my graduate studies at UT Southwestern Medical Center. I have been inspired very much by his example of enthusiasm, dedication and professionalism with regard to the work. I am grateful for the training and all he has done for me.

I would like to acknowledge Drs. Jer-Tsong Hsieh and Vikram Kodibagkar for their precious guidance and gracious help. Also I would like to acknowledge Drs. Peter P. Antich, Orhan K. Öz, Padmakar Kulkarni, and Liping Tang for their expertise, advice and time serving as my committee members. Thank Ms. Kay Emerson, Ms. Jocelyn Chafouleas, Ms. Lola Parker, and Ms. Melody Simmons for their kind assistance from many aspects.

I thank all my fellow students and colleagues, especially Peiying Liu and Mai Lin for making these years an enjoyable and learning experience in many ways.

Meanwhile, I thank the Department of Defense (W81XWH-05-1-0592; Sun) for the financial support of this research.

Finally, I wish to express my love and gratitude to my parents, my brothers, my sisters, my dearest HB and all my friends who share with me the smiles and tears, together with whom, I will always cherish and pursue my dream.

DEVELOPMENT OF IRON OXIDE BASED NANOPARTICLES AS DUAL-MODALITY IMAGING PROBES

YI GUO, M.S.

The University of Texas Southwestern Medical Center at Dallas, 2008

Supervising Professor: Xiankai Sun, Ph.D.

ABSTRACT

Dual-modality (MR/nuclear) imaging can combine exquisite anatomical resolution with superior molecular sensitivity, and significantly facilitate the accuracy of cancer diagnosis. However, the application of this technique is hampered by the paucity of sensitive dual-modality imaging probes that target tumors specifically. Here we synthesized dual-modality imaging probes by doping positron- or gamma-emitting nuclides to the core of dextran-coated superparamagnetic iron oxide nanoparticles (NUSPIONs). The synthesized nanoparticles were characterized by dynamic light scattering (DLS), transmission electron microscope (TEM), atomic force microscope

(AFM), and high performance liquid chromatography (HPLC). The evaluations of these nanoparticles were performed both *in vitro* and *in vivo*. Four radioisotopes (^{111}In, ^{177}Lu, ^{64}Cu, and ^{77}As) were successfully incorporated into the core of nanoparticles. The purification of nanoparticles via centricon filter accelerated the separation process effectively without apparent aggregation. These nanoparticles exhibited good *in vitro* stability in both phosphate buffered saline (> 99% intact) and rat serum (> 92% intact) out to 72 h, and the high r_2-to-r_1 ratio indicating their potential as MRI T_2 contrast agents. Two distinctly sized ^{177}Lu-doped nanoparticles (NUSPION-1 and NUSPION-2 with hydrodynamic radii of 11.8 ± 1.3 nm and 30.6 ± 0.5 nm respectively) were used for biodistribution studies in normal mice. NUSPION-1 showed significantly ($p < 0.0001$) higher uptake and longer retention in blood and less uptake in liver and spleen than NUSPION-2, which is advantageous for both passive and active targeting. Due to its optimal tissue distribution pattern, NUSPION-1 was chosen for further *in vivo* evaluation in PC-3 tumor-bearing mice. High tumor uptake and contrast ratios of tumor-to-muscle and tumor-to-blood were observed. A proof-of-principle dual-modality imaging study was carried out by a virtually single-dose injection in PC-3 tumor-bearing mice. The tumors were visualized by both MRI and autoradiography. Post-MRI Prussian blue iron staining and post-autoradiographic imaging biodistribution confirmed the accumulation of nanoparticles in tumors. Taken together, we have demonstrated a practical method to develop iron oxide based MRI/nuclear imaging probes.

TABLE OF CONTENTS

LIST OF FIGURES

LIST OF TABLES

PRIOR PUBLICATIONS

Jongdoo Lim, Yi Guo, Cynthia L. Rostollan, Jennifer Stanfield, Jer-Tsong Hsieh, Xiankai Sun, and Eric E. Simanek. "Biodistribution and Tumor Localization of Triazine Dendrimers". Molecular Pharmaceutics, 2008, Accepted.

Jinhai Fan, Jennifer Stanfield, Yi Guo, Jose A. Karam, Eugene Frenkel, Xiankai Sun, and Jer-Tsong Hsieh. "Effect of Trans-2, 3-Dimethoxycinnamoyl Azide on Enhancing Antitumor Activity of Romidepsin on Human Bladder Cancer". Clin. Cancer Res. 14: 1200-1207, 2008.

L, Xu; Y, Guo; Q, Liao; J, Zhang; D, Xu. "Morphological Control of ZnO Nanostructures by Electrodeposition". J. Phys. Chem. B.109 (28):13519-135223, 2005.

Manuscript titled "Development of Iron Oxide Based Nanoparticles as Dual-modality Imaging Probes" in preparation.

Abstracts:

Yi Guo, Angelo Lubag, Vikram Kodibagkar and Xiankai Sun. "Preparation of Radioisotope-Doped Iron Oxide Nanoparticles as Dual Modality Imaging Probes". Oral presentation at the Innovative Minds in Prostate Cancer Today (IMPaCT) meeting, Atlanta, GA, 2007.

Yi Guo, Zhengwang Zhang, Jian Zhou, Mai Lin, Jennifer Stanfield, Edward Tsyganov, Serguei Seliounine, Jer-Tsong Hsieh, and Xiankai Sun. "A Potential PET Imaging Probe for the Detection of Distal Prostate Cancer Metastasis". The 9th Congress of World Federation of Nuclear Medicine and Biology, Seoul, Korea, 2006.

CHAPTER 1 INTRODUCTION

Molecular imaging and cancer detection

As defined by the Molecular Imaging Center of Excellence Standard Definitions Task Force and the Society of Nuclear Medicine, molecular imaging is the visualization, characterization, and measurement of biological processes at the molecular and cellular levels in humans and other living systems (*1*). Recent advances in imaging technology aided by the explosive growth of computing power and digital image data processing have revolutionized diagnostic radiology and played pivotal roles in the development of molecular imaging. Table 1 summarizes the general features of the currently available imaging modalities that have been extensively exploited for molecular imaging studies: ultrasound (US), magnetic resonance imaging (MRI), X-ray computed tomography (CT), positron-emission tomography (PET), single photon-emission computed tomography (SPECT), bioluminescence imaging (BLI), and fluorescence imaging (FI) techniques. Together these imaging techniques allow a broad range of non-invasive visualization of biological abnormalities.

Table 1 Overview of different imaging modalities (*2-8*)

Technique	Imaging source	Resolution	Penetration depth	Sensitivity (mol/L)	Clinical use
US	High frequency sound	50 μm	mm-cm	not well characterized	Yes
MRI	Radiowaves	10-100 μm	No limit	10^{-3}-10^{-5}	Yes
CT	X-rays	50 μm	No limit	not well characterized	Yes
PET	High energy gamma rays	1-2 mm	No limit	10^{-11}-10^{-12}	Yes
SPECT	Low energy gamma rays	1-2 mm	No limit	10^{-10}-10^{-11}	Yes
BLI	Bioluminescence	3-5 mm	1-2 cm	10^{-15}-10^{-17}	No
FI	Fluorescence	2-3 mm	< 1 cm	10^{-9}-10^{-12}	Development

Imaging technologies exploit the interaction of various forms of energy with tissues for non-invasive visualization. These imaging modalities can be categorized into those that use ionizing radiation (CT, PET and SPECT) as a basis for image formation and those that do not (US, MRI, BLI, FI). Alternatively one could categorize them into imaging modalities that are capable of generating contrast without exogenous agents/probes (US, CT, MRI) and those that cannot (PET, SPECT, BLI, FI). It must be noted that in former cases, exogenous agents/probes are often needed for molecular imaging.

Ultrasound imaging, known as US scanning or sonography, uses high frequency sound waves emitted from a transducer to probe living subjects by collecting and reconstructing the reflected waves to produce 2D images. Clinical ultrasound instruments usually operate at frequencies between 7.5 and 15 MHz with a spatial resolution of 300-500 μm. At higher frequencies (40-50 MHz) the resolution can be increased to 50-100 μm but at the expense of lowering the penetration depth to 5-10 mm in soft tissues (*2*). The low cost, non-ionizing nature, ease of use, and wide availability makes ultrasound imaging a common imaging method in clinical and preclinical laboratories. The major drawback of US is its limited role in the evaluation of the organs filled with air (e.g., lungs, stomach and intestines) and hard tissues such as bone. In addition, the image quality is highly dependent on the operator and the contrast between normal and diseased tissue may be subtle (*9-11*).

Magnetic resonance imaging is based on paramagnetism of certain nuclei (typically hydrogen protons from tissue water) in a strong external magnetic field, and their interactions with other nuclei and externally applied radiofrequency waves (*2*). Because protons in different tissues have different "relaxation times" that signify interactions with the immediate surroundings, exquisite endogenous contrast can be produced between

different tissues in images. Exogenous contrast agents can be introduced as well to further enhance the tissue contrast. Using T_1 (longitudinal) contrast agents, such as Gadolinium chelates (Gd-DTPA), increases the signal intensity in T_1-weighted images while using T_2 (transverse) contrast agents, such as superparamagnetic iron oxide nanoparticles (SPIO), reduces the signal intensity in T_2-weighted images in regions where the agent is present (*2, 12, 13*). The main advantages of MRI over nuclear or optical imaging are excellent soft tissue contrast, higher spatial resolution and simultaneous extraction of the physiological/molecular and anatomical information (*5*). The disadvantages of MRI include its inherent low sensitivity, higher imaging costs, and low throughput.

X-Ray computed tomography imaging uses X-rays in conjunction with computing algorithms to generate a 3D image of an object from a series of 2D X-ray images taken around a single axis of rotation. CT images have two types of contrast: subject contrast and display contrast. CT display contrast is arbitrary because it depends only on the window level and width selected, while CT subject contrast is determined by differential x-ray attenuation in different types of tissue. Due to the inherent high-contrast resolution of CT, less than 1% of physical density differences between tissues can be distinguished. Intrinsic differences in absorption between bone, fat, air and water result in high-contrast images of anatomical structures (*14, 15*). However, unlike MRI, CT has relatively poor soft-tissue contrast, which necessitates the administration of iodinated contrast media to delineate organs or tumors (*5, 16*). Currently CT is not a molecular imaging technique yet due to the lack of target-specific contrast agents (probes) and site-specific accumulation of large quantity of such probes (*5*). In radiation therapy, CT plays a principal role in the therapy planning and the determination of radiation dose distribution (*17*).

Positron-emission tomography measures the in vivo biodistribution of imaging agents

labeled with positron emitting radionuclides. PET imaging systems detect the pairs of 511-keV photons traveling at opposite directions that are produced by positron-electron annihilation. The coincidence detection of both photons in PET within nanoseconds of each other identifies the line of response in space where the decay occurred, namely the location of the radiotracer. As one of the radionuclide-based imaging modalities, PET is highly sensitive and quantitative without tissue penetration limit. However, accurate anatomical localization of functional abnormalities is a well-known difficulty for PET. Most clinical PET scanners have a spatial resolution of 6-8 mm and small-animal scanners now have image resolutions approaching 1 mm (*2, 18-21*). Therefore, PET scans are increasingly read alongside or superimposed on CT or MRI scans giving both anatomic and metabolic information benefiting from the co-registration.

Single photon-emission computed tomography is another radionuclide based imaging technique that uses gamma ray emitters. After a subject is injected with a γ-emitting radiotracer (e.g., ^{99m}Tc, ^{111}In or ^{123}I labeled compounds) and placed in a SPECT scanner, the γ-rays are detected by gamma-cameras that rotate around the subject. The traveling directions of the emitted photons are determined by an array of lead collimators between the subject and the cameras and this direction information is used to produce tomographic images. Optimal collimator design requires a compromise between the spatial resolution and the sensitivity of a SPECT system. Because of the use of collimators for the definition of the angle of incidence, the sensitivity of SPECT is often lower than PET (*5*). The advantages of SPECT are similar to those of PET. Current SPECT systems generally allow dual-isotope imaging protocols, in which two tracers labeled with different isotopes, are used to probe two distinct biological events simultaneously (*2, 5, 22, 23*).

Bioluminescence imaging is an optical imaging technique that utilizes light emission due to oxidation of systemically administered luciferin in presence of an enzyme, luciferase, produced by exogenously transfected cells. BLI is a highly sensitive technique that is particularly well suited to long-term, longitudinal studies in cultured cells and small animals. It has a particularly strong impact on preclinical studies of tumor progression. As a reporter gene imaging technique, its applications have been seen in studies of circadian rhythmicity at the level of whole organisms, explanted tissues, and even single cells (*24-28*). However, BLI is unlikely to be translated into clinical studies, owing to the inherent light penetration limit and the fact that a stable expression of luciferase (or an analogous system) is required to generate the signal (*25-27*).

Fluorescence imaging is also an optical imaging technique that uses fluorescence and phosphorescence instead of bioluminescence. An external light of appropriate wavelength is used to excite a fluorescent molecule, which immediately emits longer-wavelength, lower-energy light for imaging. Probes for fluorescence imaging may be endogenous molecules (such as collagen or hemoglobin), fluorescent proteins (such as red or green fluorescent proteins), or optical contrast agents with fluorescent molecules. Reflectance fluorescence imaging (*29*) and fluorescence-mediated molecular tomography (FMT) are the two most common approaches currently used to probe deep tissues (*2, 3, 27, 30-33*). Similar to BLI, FI has the exceptionally high sensitivity but its application is limited by the penetration depth and the requirement (in some cases) of exogenously transfected genes in the tissue of interest.

In summary, each imaging modality has its own advantages and disadvantages. A perfect imaging technique that could furnish anatomic, physiologic, and molecular information with high sensitivity and specificity doesn't exist. To date hybrid imaging systems (e.g.,

PET/CT, SPECT/CT, and PET/MRI, etc.) have been seen to rapidly outdate single modality devices in clinical practices and preclinical research. Obviously this trend requires the development of corresponding multi-modality imaging probes.

Nanoparticles in molecular imaging and drug delivery

Due to the recent advances of nanotechnology, varieties of nanoparticles have become available for biomedical applications, such as polymeric (*34-39*) and magnetic nanoparticles (e.g., SPIO) (*40-50*), liposomes (*39, 51-58*), solid lipid particles (*39, 59, 60*), micelles (*29, 51-55*), quantum dots (*61-68*), dendrimers (*53, 58, 69-73*), and other nanoassemblies (*48, 74, 75*). Among them, SPIO nanoparticles have drawn extensive attention in the field of molecular imaging mainly due to their negative enhancement effect on T_2- and T_2*-weighted MR imaging, low toxicity (if any), and the ease of their surface functionalization (*76*).

SPIO-based nanoparticles for molecular imaging

SPIO-based nanoparticles currently constitute a large group of MRI contrast agents. The nano-sized contrast agents typically comprise a nanosized SPIO core and a variety of hydrophilic coating materials such as polysaccharide (e.g., dextran), polymer (e.g., poly ethylene glycol: PEG), etc. Table 2 shows a list of SPIO-based nanoparticles that are commonly used in clinical and preclinical laboratories.

SPIO-based nanoparticles lack explicit molecular specificity for imaging of biological pathways and thus they are usually taken up by organs of reticuloendothelial system (RES) and macrophages. Therefore, SPIO-based MRI agents are used for liver, spleen, lymph node and macrophage imaging (*41*). The liver imaging by using these particles results from the non-specifically taken up by Kupffer cells in the healthy liver, while the lymph node imaging takes advantage of the extravasation of nanoparticles from the

vasculature to the interstitial space where they are transported to the lymph nodes via the lymphatic vessels. Since macrophages are rich in healthy lymph nodes but not in metastatic nodes (*76*). SPIO has been successfully used to detect clinically occult lymph-node metastases in human patients by MRI (*77*). Aided by the lymphotropic SPIO, the MRI sensitivity of the diagnosis was increased from 45.5% to 100% with a specificity of 95.7% on a patient-by-patient basis. When the lymph node sizes were in the range of 5-10 mm, the sensitivity was improved from 28.5% to 96.4% with a specificity of 99.3%. However, when the lymph node size was smaller than 5 mm, the sensitivity decreased dramatically to 41.8%. It might be possible to use lymphotropic superparamagnetic nanoparticles aided MRI to detect small metastases (1-2 mm), nevertheless it is unclear whether the technique would reliably identify small metastatic foci in nodes that are partially replaced by tumor (*78*).

One hypothesis of our project is to improve the detection sensitivity of the SPIO-aided MRI by doping positron- or gamma-emitting isotopes into the core of SPIO, thus enabling PET or SPECT imaging, which would add the superior sensitivity of nuclear imaging techniques to the exquisite resolution of MRI.

Table 2 SPIO-based nanoparticles marketed or under clinical investigations (*49, 76, 79, 80*)

Agent	Hydrodynamic diameter (nm)	Coating	Comment
Ferumoxides AMI25	120-180	Dextran T10 KDa	FDA-approved liver imaging agent; Cellular
Ferumoxytol C7228	35	Carboxymethyl dextran T10 KDa	FDA-approved liver imaging agent; Blood pool
Ferumoxtran-10 AMI 227	15-30	Dextran T10 KDa, T1 KDa	Liver imaging (phase 3 trials completed)
Ferucarbotran A SHU555A	65	Carboxydextran T1.8 KDa	Liver imaging; Cellular imaging
Ferucarbotran C SHU555C	20	Carboxydextran T1.8 KDa	Blood pool agent; Cellular imaging
CLIO-TAT peptide	30	Dextran periodate	Experimental nanoparticle for targeted imaging
VSOP C-184	8.6	Citrate	Liver imaging; Blood pool agent;

The Weissleder group has extensively exploited SPIO-based nanoparticles to develop MRI contrast agents and multimodality imaging agents (*81*). In the past decade, a series of dextran-coated cross-linked iron oxide nanoparticles (CLIO) with primary amine groups on the surface have been reported by the group for various applications including *in vivo* detection of cancer by dual-modality imaging approaches (MRI/Optical).

Recently DeNardo and coworkers reported ^{111}In-antibody-linked iron oxide nanoparticles (^{111}In-ChL6 nanoparticle) for the thermoablative therapy of human breast cancer xenografts in mice (*82*). Inductively heating the nanoparticles with an alternating magnetic field (AMF) caused the tumor necrosis. SPECT imaging was performed to quantify the accumulation of nanoparticles in the tumor site, which was about 14 %ID/g at 48 h post injection (p.i.). These ^{111}In-ChL6 nanoparticles may have the potential to be used for dual-modality (MR/SPECT) imaging.

Common approaches to SPIO-based nanoparticle preparation

To date, many methods have been reported to prepare nano-sized iron oxide, such as wet chemical (*83-86*), electrochemical (*87*), sonochemical (*88*), and pyrolysis techniques (*89, 90*). Among them, a wet chemical technique invented by Weissleder and colleagues is most commonly used due to the ease of surface modifications for various applications (*3, 91-100*).

Nanoparticles naturally tend towards coagulation and aggregation (*101*). This tendency could be minimized by nanoparticle surface modifications using polymers (e.g., PEG, dextran) or by adding surfactants (e.g., Tween 20 or Tween 80). Among the used coating molecules, dextran is most commonly used for the SPIO-based nanoparticle preparation. PEGylation is also an effective way to optimize the pharmacokinetics of the nanoparticles, which can provide improved solubility, biocompatibility, and prolonged circulation time (*44, 54, 101-109*).

A general procedure to prepare functionalized SPIO-based nanoparticle involves three steps: (1) simultaneous dextran coating during the coprecipitation; (2) shell cross-linking; and (3) functionalization of the nanoparticle surface.

Tumor targeting strategies for SPIO applications

Tumor targeting of SPIO-based nanoconjugates can be achieved by either passive or active targeting mechanisms. The passive-targeting approach takes advantage of the so called enhanced permeability and retention (EPR) effect (*110-112*). During tumor angiogenesis, rapid vascularization in fast-growing cancerous tissues is known to result in leaky, defective architecture and impaired lymphatic drainage which allows the extravasation and accumulation of nanoparticles in the interstitial tumor space. The extravasation of nanoparticles from the circulatory system is highly dependent on particle

size. Therefore, the nanoparticle size and surface properties are critical to avoid the uptake by RES systems in the liver and spleen (*52, 113, 114*).

To minimize the non-specific uptake, the active targeting can be performed by attaching targeting agents to the nanoparticle surface via various conjugation chemistries (*65, 115, 116*). The active targeting strategies normally exploit the existence of molecular signatures on cell membranes. In general, cancer cells of a specific tumor overexpress specific receptors or antigens. Therefore it is straightforward to conjugate specific ligands that bind to the receptors or antigens with nano-structures for active targeting. The targeting molecules can be broadly classified to proteins (monoclonal antibodies and antibody fragments), peptides, nucleic acids (aptamers), and small organic molecules. In addition, nanoparticle surface can be conjugated with multiple ligands and the consequent multivalent binding to target molecules could result in dramatically increased uptake and retention of the particles (*102, 117*). To date, a variety of nanoparticles including SPIO-based nanoparticles have been functionalized with small molecules, peptides, and antibodies targeting endothelial receptors on the microvasculature of proliferating tumors (*118-122*). Here several commonly used targeting molecules that have been reported to construct iron oxide based nano-conjugates for targeted imaging or therapy of cancers are presented.

Targeting prostate-specific membrane antigen (PSMA)

PSMA is a type II transmembrane glycoprotein overexpressed about a thousand-fold on prostate cancer (highly restricted to the prostate epithelium) and neovasculature of most solid tumors, but not in the vasculature of the normal tissues (*123-128*). Minimal expression is observed in the brain and kidneys. Because it is a cell surface protein that presents a large extracellular domain (amino acids 44-750), PSMA has been utilized as

target for monoclonal antibody directed imaging agents or therapeutics for prostate cancer (*123, 128, 129*). Indeed, the only FDA approved prostate cancer imaging agent was an ^{111}In-labeled PSMA monoclonal antibody (7E11-C5.3) (*123, 128*). Previous clinical trials showed that this agent had improved sensitivity in the detection of prostate over CT or MRI, and it could be used to define the stage of localized prostate cancer and metastases, when used in conjunction with CT or MRI (*128*). However, recent reports indicate that it has problems in terms of specificity and sensitivity because the antibody (7E11-C5.3) recognizes an internal epitode (the first six amino acids) of PSMA (*123*). As a result, several research groups have developed monoclonal antibodies (e.g., J591, J533, J415, E99, and E6, etc.) that recognize epitodes within the extracellular PSMA domain (*129-134*). These antibodies have shown significantly improved sensitivity and specificity in the detection of prostate cancer. In addition, a ligand screening technology, SELEX (systematic evolution of ligands by exponential enrichment), has been utilized to select nuclease-stabilized oligonucleotides, namely aptamers, which bind tightly and specifically to a given ligand (*135-142*). Because most aptamers are much smaller than antibodies and don't have immunogenicity, they have been claimed as a new class of molecules that can contest the roles of antibodies in imaging, diagnostics and therapeutics (*143, 144*). In 2002, this technology was firstly used to screen RNA aptamers that bind to PSMA. Two such aptamers (xPSM-A9 and xPSM-A10) were identified with high binding affinity to the extracellular domain of PSMA. Truncated version of xPSM-A10 (minus 3 × 5 nucleotides) retains the binding ability and it was named xPSM-A10-3 (*145*). Langer's laboratory immediately used xPSM-A10-3 to construct nanoparticle-aptamer bioconjugates for targeting prostate cancer, and showed that the nanoconjugates can efficiently target and get taken up by LNCaP epithelium cells. In contrast, the uptake of

the nanoconjugate was not enhanced in PC-3 epithelium cells that don't express PSMA (*146*). Recently, Serda et al. reported a specific and sensitive MRI method to detect both local and metastatic prostate cancer by attaching an anti-PSMA antibody (MLN59) to iron oxide nanoparticles (*147*).

Targeting the folate-receptor (FR)

One of the two existing cellular folate transport systems, the folate receptor is a membrane-associated folate-binding protein that is overexpressed on a number of tumor cells (e.g., ovarian, colorectal, breast, nasopharyngeal carcinomas, etc.) and limitedly expressed in most normal tissues (*148, 149*). Because FR binds physiologic folates with affinity in the nanomolar range (*148*), it is an attractive molecular target for cancer imaging and therapy (*150-153*). Since folate intake is essential for cell life, FR-mediated endocytosis of folate-conjugate molecules delivers the cargo to the cytosol rather than to lysosomes for destruction (*154*). In this process, the folate-conjugated drug interacts with the membrane receptor first, then the FR-complex enters the cell, and the cargo is released. Eventually, the receptor is recycled back to the cell surface where it can interact with more folate. Choi et al. and coworkers (*155*) synthesized the folate-FITC-iron oxide nanoparticles which were delivered to the receptor-expressing tumors (KB tumors) for *in vivo* MRI. The results showed a T_2 MRI intensity decrease in tumor at 2.5 h p.i.

Targeting the integrin $\alpha_v\beta_3$ – the vitronectin receptor

In cancer, the progression rate of a solid tumor is strongly dependent on its ability to stimulate angiogenesis, a process in which new blood vessels grow from pre-existing vessels to supply tumor cells with oxygen and essential nutrients. In 1994, Cheresh and coworkers reported that the integrin $\alpha_v\beta_3$ becomes highly upregulated on activated endothelial cells in the chick CAM (*156, 157*) and plays a critical role in the survival of

endothelial cells, while its expression is weak in most normal organ systems. Since then the integrin $\alpha_v\beta_3$ (the vitronectin receptor) has been studied extensively and identified as an important receptor affecting tumor growth, local invasiveness, and metastatic potential (*158*). Among over 25 identified integrin receptors, about two thirds including integrin $\alpha_v\beta_3$ recognize and bind tightly to the tripeptide sequence Arg-Gly-Asp (RGD). In addition, numerous synthetic RGD peptido-mimetics have been developed as $\alpha_v\beta_3$ antagonists (*159-161*). The RGD-containing peptides are usually cyclized (e.g., via disulfide linkage) before use as $\alpha_v\beta_3$ antagonists, because the cyclic peptides show significantly improved potency (*162-164*) and higher resistance to chemical degradation *in vivo* than their linear counterparts in inhibiting tumor angiogenesis (*165*). Montet et al. (*166*) reported a dual-modality (MR/optical) imaging probe cRGD-CLIO (Cy5.5) which was synthesized by conjugating the amino cross-linked iron oxide (CLIO) with disulfide-linked cyclic RGD peptide (cRGD), followed by the attaching the fluorochrome (Cy5.5) directly to the CLIO. For the *in vivo* evaluation, two tumor models were used, one implanted with BT-20 (a human breast carcinoma cell line expressing the $\alpha_v\beta_3$ integrin) and the other implanted with 9L (a rat gliosarcoma cell line without the expression of $\alpha_v\beta_3$ integrin). The results demonstrated that these magneto-fluorescent RGD nanoparticles were targeted to the $\alpha_v\beta_3$-expressing tumor *in vivo* and were detectable by fluorescence reflectance imaging, fluorescence molecular tomography, and MRI. Recently, Zhang et al. (*167*) reported the RGD coupled USPIO probes for tumor angiogenesis targeting. Impressively, these probes could distinguish tumors differing in the degree of $\alpha_v\beta_3$ integrin expression and the angiogenesis profile by MRI.

Targeting HER-2 receptor

Molecular classification of breast cancer is generally based on the presence or absence of estrogen receptor-α (ER): hormone-positive or -negative; and the status of HER-2 receptor: HER-2-positive (or amplified) or -negative (or non-amplified (*168*). Now there is a growing appreciation of the molecular information, which can aid in the planning of specific treatment methods for patients in each distinct class (*169-171*). Overexpressed in 20-30% of all breast cancers, HER-2 is a member of the human epidermal growth factor receptor (HER) family including the epidermal growth factor receptor (HER-1/EGFR), HER-2, HER-3, and HER-4 (*172*). The overexpression of HER-2 in breast cancers associates with greater metastatic potential and higher resistance to some types of chemotherapy indicative of poor long-term survival rates of patients. Wild-type HER receptors comprise three domains: an extracellular domain for ligand binding and interacting with other HER receptors; an intracellular domain for tyrosine kinase activity and regulatory functions (e.g., growth and differentiation of cells), and a transmembrane domain (*172*). Due to its clinical relevancy, HER-2 has become one of the major targets in the treatment of breast cancers (*173-179*). To date, however, no known ligand for HER-2 receptor has been discovered, suggesting that it serves as a coreceptor to form heterodimer complexes with other three HER family members upon their specific ligand binding (*169*). This dimerization results in the activation of HER tyrosine kinase thus facilitating cell proliferation, invasion, and antiapoptosis (*180*). Trastuzumab (Herceptin®), a humanized IgG monoclonal antibody that targets the extracellular domain of HER-2, has been approved by the US FDA to treat metastatic breast cancers or be used as a therapeutic adjuvant. A few other HER-2 targeting monoclonal antibodies such as pertuzumab are currently in clinical trials, so are several HER-2 antagonists (*172, 180*). Not surprisingly, anti-HER-2 antibodies and their fragments have been explored for

non-invasive imaging studies of cancers (*29, 181-186*). To date anti-HER-2 antibodies have been used to direct iron oxide nanoparticles for *in vitro* and *in vivo* studies (*181, 187-190*).

Prostate cancer and common diagnosis methods

More than 7,000,000 cancer deaths occur worldwide and more than 500,000 deaths occur in the United States each year (*191, 192*), among which prostate cancer becomes the second only to lung cancer as a leading cause of cancer-related deaths in men in the United States (*193*). According to the American Cancer Society's estimation, 218,890 new cases of prostate cancer would be diagnosed and 27,050 men would die of this disease in 2007 (*194, 195*).

Currently, prostate cancer can be characterized by its clinical tumor/nodes/ metastasis (TNM) stage, Gleason grade, and prostate specific antigen (PSA) serum level (*196*). PSA testing was first approved in 1986 for the detection and recurrent disease in patients with established prostate cancer. As a routine test for prostate cancer screening, however, PSA levels can not discriminate between benign and malignant prostate conditions, which results in up to 700,000 unnecessary prostate biopsies each year in the United States (*197*). Furthermore, although PSA levels historically correlate with the presence of prostate cancer, they provide very limited information regarding the location and extent of cancer (*197, 198*).

Transrectal ultrasound (TRUS) is a well known and most widely used clinical imaging method, which is also the standard imaging tool for prostate cancer biopsy guidance and brachytherapy seed placement (*195*). However, TRUS can not warrant a definitive stage of prostate cancer due to the isoechoic property of prostate cancer that is indistinguishable from the surrounding tissues (*199*). On the other hand, conventional

imaging techniques like radionuclide bone scans, US, CT scans, and MRI have played quite limited part in the diagnosis, staging, and monitoring of prostate cancer patients (*199*). Therefore it is of great importance to develop new non-invasive imaging techniques with high sensitivity and specificity for the detection and monitoring of prostate cancer.

The major goal of prostate cancer imaging is to characterize the disease more accurately and obtain comprehensive anatomic, functional and molecular information and thus to identify new metabolic markers and better understand how they regulate prostate cancer aggressiveness and cellular proliferation (*195*). PSMA, a cell surface membrane protein, is one of the most extensively studied prostate cancer markers (*200*). However, PSMA is not a specific biomarker for prostate cancer (*201*). Further more, a series of reports suggest that prostate cancer is a multifocal disease mixed with a heterogeneous cell population of androgen dependent (dependent on androgen for survival), androgen-sensitive (stimulated by androgen but not dying in their absence), and androgen independent (neither stimulated nor dying in the presence or absence of androgen) cells (*202*), out of which only androgen responsive cells express PSMA (*203-205*). In this project, we explore a new way to target prostate cancer.

Targeting prostate cancer by a cell-permeable peptide (CPP)

Recent development of CPPs offers a new avenue of cancer targeting and therapy because CPPs are able to self-translocate across biological membranes as delivery vehicles that carry different functional cargos, such as proteins/peptides, DNA/RNA, liposome and nanoparticles (*206-208*). CPPs can be categorized into (1) basic amino acids e.g., Tat protein and polyarginines; (2) amphiphilic peptides composed of basic amino acids and hydrophobic amino acids; e.g., *Drosophila* antennapedia protein (penetratin); (3) a

chimera peptide of a neuropeptide galanin and a bee toxin peptide mastoparan; (4) the hydrophobic segment derived from the extracellular secretion peptide of the Kappori fibroblase growth factor.

To date, the exact mechanism of each CPP uptake has been still unclear. In some literatures, it appears that cell membrane proteoglycan or glycoprotein could play an important role in mediating CPP uptake (*209*-*212*). Also, it has been noticed that the live cells produce punctuate signals of the peptides under microscopic observations (*209*). These facts suggest the significant contribution of endocytosis to the cellular uptake of CPP, particularly, the basic amino acid peptides. However, it has also been reported that the typical inhibitors of classical endocytosis do not have a notable effect on the cellular uptake of these peptides and that the cellular localization of polyarginine peptides are not necessarily the same as that of transferrin. The involvement of different types of endocytoses from classical clathrin endocytoses to macropinocytes has been suspected; different internalization pathways including clathrin endocytosis (*213*), caveolae endocytosis (*214*), and Golgi-mediated transport (*215*) have also been documented for different kinds of CPP. Alternatively, macropinocytosis is a pathway of cellar uptake in which the polymerization of actin filaments makes the plasma membrane thrust out from the cell surface. This procedure is in contrast to that of classical clathrin endocytosis with the formation of concave structures on the plasma membranes. Using macropinocytosis inhibitor EIPA (5-(*N*-ethyl-*N*-isopropyl) amiloride), a greater inhibition effect to R16 than R8 was observed (*209, 216*). In addition, other factors such as cell surface glycosaminoglycans (*216, 217*) have been demonstrated to play an important role in the cellular uptake of arginine peptides because electrostatic interaction of the arginine peptides with these negatively charged proteoglycan will make these peptides condense

on the cell surface, and this would eventually accelerate the cellar uptake of these peptides.

Although the cell internalization mechanism of CPP is still under debate, they have not been reported to have tissue specificity. During the screen of CPPs for optimal intracellular delivery of a proline-rich domain for prostate cancer therapy, we found out that an arginine-rich peptide (R11) accumulated preferentially in prostate and bladder tissues (**Figures 1** and **2**).

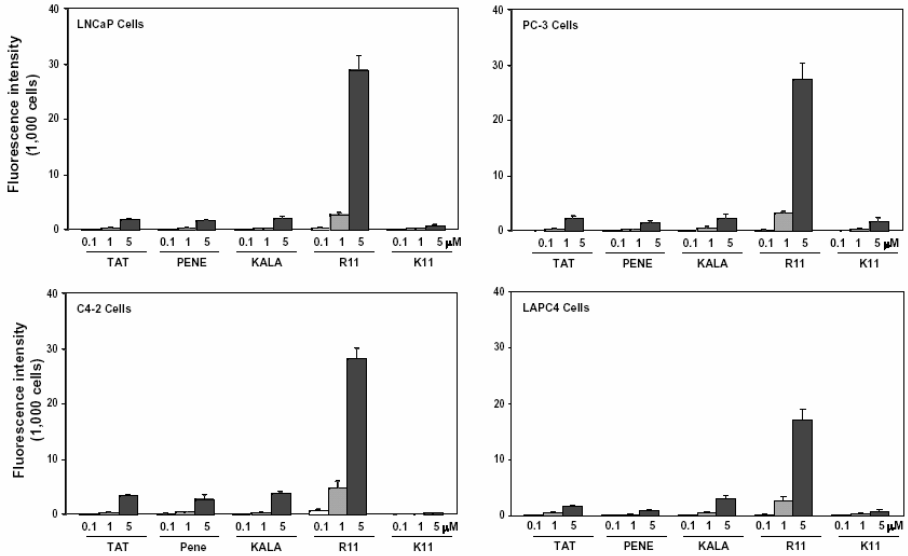

Figure 1. Internalization of five CPPs (TAT, PENE, KALA, R11, and K11) to four prostate cancer cell lines (LNCaP, C4-2, LAPC4 and PC-3 cells).

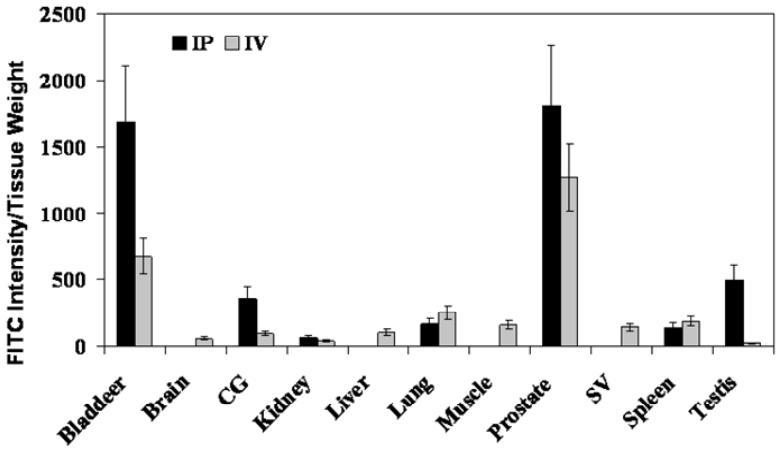

Figure 2. FITC-tagged R11 in nude mice (24 h p.i., n=3). The peptide was administered

via intra-peritioneally (IP) or intra-venous (IV) route.

In order to explore this peptide for the detection of the prostate cancer *via* PET, we conjugated R11 with DOTA (1, 4, 7, 10-tetraazacyclododecane-1, 4, 7, 10-tetraacetic acid) for ^{64}Cu labeling. Biodistribution of ^{64}Cu-DOTA-R11 in both normal and tumor-bearing mice were performed. From the biodistribution results (shown in Chapter 3), it is apparent that ^{64}Cu-DOTA-R11 has a strong tendency to accumulate in prostate and bladder. Further, this peptide exhibited remarkably low uptake in other organs (e.g., blood, lungs, liver, spleen, kidneys, and muscle). This confirms the observation of using FITC tagged R11 in the same animal model, and indicates that R11 could be a novel biomarker for PET imaging probe development.

We reason that by conjugating R11 with our nanoparticles, the targeted delivery efficiency could be significantly enhanced due to the so called multivalent effect resulted from the multi-presentation of R11 on the nanoparticle surface in addition to the R11-facilitated cellular internalization.

Significance of this study

Because each imaging modality has its own inherent limitations, developing a probe that can be used in multiple imaging modalities appears highly desirable and attractive. It is feasible and plausible to use nanoscaffolds for such developments because multi-presentation of various functionalities can be conveniently made possible on a common platform. Indeed it has been reported that the iron oxide nanoparticles could be developed as MRI/optical dual imaging probes by coupling with a fluorescent tag for highly detailed anatomic (MRI) and molecular information (near-infrared (NIR) optical imaging) in living organisms (*92*). However the feasibility has been demonstrated, simultaneous *in vivo* dual-modality imaging of the tumor targeting of such probes had not

been achieved until recently a multifunctional SPIO-based probe was reported (*218*). The probe was constructed by conjugating three different functional molecules to the dextran surface of SPIO nanoparticles: an NIR dye (Cy5.5) for NIR fluorescence imaging (NIRF), siRNA molecules (siGFP or siSurvivin) and a membrane translocation peptide (MPAP) for proof-of-concept intracellular delivery therapeutic siRNA molecules. Further a high density of apoptotic nuclei was observed in the tumors treated by the probe carrying siSurvivin (*218*). This beautiful work convincingly demonstrates that non-invasive dual-modality imaging and therapeutic siRNA delivery can be accomplished by using a nanoscaffold. However, the sensitivity of MRI or NIRF in this dual-modality imaging approach was not addressed. In addition, the NIRF technique can be hardly translated into clinical practice due to the inherent tissue penetration problem of optical imaging.

In this thesis, we have successfully developed an approach to make SPIO-based dual MRI/SPECT or MRI/PET imaging probes, which are poised to overcome the aforementioned problems while maintaining the multifunctional features. The detailed method is presented in the following Chapters. Briefly, our multifunctional nanoscaffolds were prepared by incorporating gamma- or positron-emitting nuclides to the core of dextran-coated SPIO nanoparticles (NUSPIONs). Through the control of the incorporation amount of radioisotope, the sensitivity of the nuclear imaging modality (SPECT or PET) can be tuned to visualize small tumor metastases (< 5 mm) that SPIO-assisted T_2-weighted MRI would miss (*78*) for a broad range of prostate cancer metastasis detection. Other advantages of this approach include 1) the incorporation of radioisotopes into the nanoparticle core offers an intact surface for further modifications if targeting and/or drug loading are needed; 2) No bifunctional chelators, such as TETA

and DOTA, are needed as in conventional radiolabeling of nanoparticles. This avoids the concerns on *in vivo* transchelation of metal ions from the chelators/nanoparticles, which has been well documented in the literature (*219-221*), and thus ensures the integrity of the dual modality imaging probes *in vivo*; and 3) It was recently reported that 5 mol% substitution of iron in the SPIO core with trivalent lanthanide did not affect the magnetic, physical, and chemical characteristics of the iron oxide nanoparticles (*222*). Therefore, it is straightforward to extend the application of our proposed multifunctional probes to radiotherapy as necessary by loading more radioisotopes to the nanoparticle core.

Based on a wet chemical technique invented by Weissleder and colleagues (*3, 91-99*), our synthetic approach was developed. However when working with radioisotopes, we are constrained by time. The major and critical challenge that faced us was how to efficiently incorporate radioisotopes into the nanoparticle core within a reasonable timeframe (< two half lives of the isotope). To date we have established standard operation procedures for the preparation of NUSPIONs. Four typical nuclear imaging isotopes in Table 3 have proven to yield high incorporation rates (> 58%).

Table 3. Decay properties of radioisotopes used for NUSPION preparation (*223*)

	SPECT Isotopes		**PET Isotopes**	
	^{111}In	^{177}Lu	^{64}Cu	^{74}As*
Half Life	2.83 d	6.71 d	12.70 h	17.77 d
Decay	γ (0.171 MeV), 90% γ (0.245 MeV), 94% β^- (0.145 MeV), 8% β^- (0.219 MeV), 5%	γ (0.208 MeV), 11% γ(0.113MeV), 6.4% β^- (0.497 MeV), 79%	β^+(0.65 MeV), 19% EC, 41% β^- (0.579 MeV), 38%	β^+(0.94 MeV), 26% EC, 37% β^- (0.71 MeV), 16%

*^{77}As was used due to the high cost of ^{74}As in the preliminary experiments.

CHAPTER 2 EXPERIMENTAL PROCEDURES

Materials

All chemicals, solvents, and reagents were purchased from Sigma-Aldrich and used as received unless otherwise noted. NH_2GR11 (MW: 1792 Da) was synthesized from the Peptide Synthesis Laboratory of UT Southwestern Medical Center (Dallas, TX). Dextran T10 (MW: 10 KDa) was purchased from Pharmacosmos A/S (Holback, Denmark). Ammonium hydroxide water solution (puriss. wt. 29.46%) was purchased from Fisher (Houston, TX). Dialysis tubing (MWCO 100 KDa) was purchased from Spectrum Laboratories (Rancho Dominguez, CA). Instant thin-layer chromatography (ITLC) SG plates and acrodisc syringe filter were purchased from Pall Life Sciences (East Hills, NY). Arsenic-77 was produced at a non-carrier added (nca) state via the ^{76}Ge (n, c) 77Ge ($t_{1/2}$:11.30 h) $\rightarrow$ ^{77}As reactions in the TRIGA reactor at the University of Texas at Austin; $^{177}LuCl_3$ in 0.05 N HCl was purchased from the University of Missouri Research Reactor (Columbia, MO); $^{111}InCl_3$ in 0.05 N HCl from Trace Life sciences (Denton, Texas, USA), and $^{64}CuCl_2$ in 0.1 N HCl from MDS Nordion (Canada) or Trace Life sciences. Super sharp diamond-like carbon (DLC) tips were purchased from Nanotech-America (Allen, TX). Mica Grade V-1 15 mm x 15 mm x 0.15 mm substrate was purchased from SPI Supplies and Structure Probe, Inc (West Chester, PA). Centricon filters (YM-100: MWCO 100 KDa) were purchased from Millipore (Billerica, MA). C-18 Sep-Pak cartridges were purchased from Waters (Milford, MA). T-medium, fetal bovine serum (FBS) and matrigel were purchased from Invitrogen Corporation (Grand Island, NY), Gemini Bio-Products (Woodland, CA), and BD Biosciences (Bedford, MA), respectively. Normal male Balb/c (4-5 weeks of age) and nu/nu mice (5-7 weeks of age) were purchased from Harlan (Indianapolis, IN). Milli-Q water (18 MΩ-cm) was obtained from a Millipore Gradient

Milli-Q water system (Billerica, MA). All aqueous solutions were prepared in deoxygenated Milli-Q water 30 min prior to use.

Tissue culture and animal model

The PC-3 or T-24 cell lines were obtained from the American Type Culture Collection (ATCC, Manassas, VA). The cells were cultured in T-media at 37 °C in an atmosphere of 5% CO_2 and were passaged at 75% confluence in P150 plates. T-Media was supplemented with 5% FBS and 1 × Penicillin/Streptomycin. Cultured cells were harvested from monolayer using PBS and trypsin/EDTA, and suspended in T-media with FBS. The cell suspension was then mixed 1:1 with Matrigel and injected subcutaneously (1.5×10^6 cells per injection, injection volume 100 μL) into both rear flanks of nu/nu mice. After the cell injection, the animals were monitored three times a week by general observations. The tumors were noticed to grow in the first week and allowed to grow about one month when they became palpable but were under 100 mg.

Radiolabeling and *in vivo* evaluation of R11 (NH_2GR11)

Radiolabeling of DOTA-R11

NH_2GR11 was first conjugated with a bifunctional chelator DOTA, in order to be radiolabeled with ^{64}Cu. To a 1.5 mL vial containing 20 μg DOTA-R11 in 100-200 μL of 0.1 M NH_4OAc (pH = 6.5), 1-2 mCi of ^{64}Cu in 0.05 N HCl was added. The reaction mixture was mixed and incubated at room temperature (RT) for 1 h. Then 5 μL of 5 mM DTPA (diethylene triamine pentaacetic acid) was added to the reaction vial and allowed to incubate for 5-10 min. The ^{64}Cu-DOTA-R11 was separated from ^{64}Cu-DTPA by a C-18 cartridge. Radio-TLC analysis was performed on a Rita Star Radioisotope TLC Analyzer (Straubenhardt, Germany) to monitor the radiolabeling reaction. High performance liquid chromatography (HPLC) and radio-HPLC were performed to determine radiochemical

purity of the products on a Waters 600 Multisolvent Delivery System equipped with a Waters 2996 Photodiode Array (PDA) detector and an in-line Shell Jr. 2000 radio-detector (Fredericksburg, VA).

Biodistribution studies of DOTA-R11

All animal studies were performed in compliance with guidelines set by the UT Southwestern Institutional Animal Care and Use Committee. The biodistribution studies were performed in normal mice, PC-3 (prostate tumor) and T-24 (bladder tumor) tumor-bearing mice. The injected dose of ^{64}Cu-DOTA-R11 in the biodistribution studies was in range of 5-10 μCi. The animals were sacrificed at specific time points (n = 4 at each time point). Organs of interest (blood, lung, liver, spleen, kidney, testis, prostate, bladder, seminal vesicle (SV), coagulation gland (CG), muscle, femur, tibia, or tumor and brain) were removed, weighed, and counted. The blood was collected from the retroorbital sinus of the animals at 5 min, 10 min and 20 min p.i. for the evaluation of pharmacokinetic parameters. Standards were prepared and counted along with the samples to calculate the percent injected dose per gram tissue (%ID/g).

Synthesis of CLIONPs

Cross-linked dextran-coated iron oxide nanoparticles (CLIONPs) were prepared via the coprecipitation of Fe^{3+} and Fe^{2+} from an aqueous solution by the addition of a base solution, which was modified from published procedures (*105, 224, 225*). Briefly, 58-60 mg (~ 0.22 mmole) of $FeCl_3 \bullet 6H_2O$, 22-23 mg (~ 0.11 mmole) of $FeCl_2 \bullet 4H_2O$, and dextran T10 were dissolved in 50 mL of deoxygenated Milli-Q water, giving a clear light yellow solution. From the resulting solution (pH ~ 3), 20 mL was taken out and transferred to a reaction flask, which was then stirred at a speed of 600 rpm in an ice/water bath. The inert atmosphere was maintained by a nitrogen (N_2) flow at 3 liters

per minute (LPM). To the 20 mL of Fe^{3+}/ Fe^{2+}/ dextran solution, 1 mL of 6.45% ammonia was added drop-wise by a syringe pump in a 10 min period, during which the color of the reaction mixture changed from light yellow to light green to dark green. At the end of the ammonia addition, the pH was around 10. The reaction mixture was kept in the ice/water bath for 30 min, and then gradually heated by an oil bath to 75-80 °C in 1 h. At the same time, the N_2 flow rate was decreased to 1 LPM.

The dextran shell cross linking was done by adding 7 mL Milli-Q water, 6 mL of 5 M NaOH, and two portions of epichlorohydrin (3 mL followed by 2 mL with a 30 min interval) to the above reaction mixture that was cooled down to RT. The cross linking reaction was allowed to proceed 2 h with constant stirring at 600 rpm under N_2 protection. The resulted reaction mixture was concentrated and then washed four times with water by centricon filter tubes (MWCO: 100 KDa) to remove nonreacted reagents and excess dextran molecules. Another dextran (MW 64-76 KDa) was initially used to optimize the synthesis conditions. Factors such as concentration, pH, temperature, and incubation time were evaluated.

Preparation of NUSPIONs

Four radioisotopes were used in this project for the preparation of nuclides incorporated NUSPIONs: ^{77}As ($t_{1/2}$ = 38.8 h), ^{177}Lu ($t_{1/2}$ = 6.7 d), ^{111}In ($t_{1/2}$ = 2.8 d), and ^{64}Cu ($t_{1/2}$ = 12.7 h). By introducing the radioisotopes to the core of nanoparticles, we anticipate to obtain dual-modality imaging probes for anatomical MRI and functional nuclear imaging. Similar to the preparation of CLIONPs, incorporation of radioisotopes was achieved by their simultaneous precipitation with the iron salts. Briefly, 58-60 mg (~ 0.22 mmole) of $FeCl_3 \bullet 6H_2O$, 22-23 mg (~ 0.11 mmole) of $FeCl_2 \bullet 4H_2O$, and dextran T10 were dissolved in 50 mL deoxygenated Milli-Q water, giving a clear light yellow solution. To the 20 mL

of Fe^{3+}/ Fe^{2+} / dextran solution, 1-2 mCi of a radioisotope in 0.05 N HCl was added. Then 1 mL of 6.45% ammonia was added drop wise by a syringe pump. The following cross linking and purification was the same as in the cold nanoparticle preparation except that after the completion of cross linking reaction, 5 mL of 5 mM DTPA was added to the reaction mixture which was stirred for another 10 min prior to the purification by centricon filters. The synthesis is schematically shown in **Figure 3**.

Reaction conditions as aforementioned were also evaluated to prepare two distinct ^{177}Lu-doped NUSPIONs with different sizes for further *in vitro* and *in vivo* studies. The main determinant in the controlling of nanoparticle size appeared to be the T10 dextran amount added for the reaction. To synthesize the smaller ^{177}Lu-doped NUSPIONs (NUSPION-1), 5 g of T10 dextran was added to the 50 mL reaction mixture, while for the larger one (NUSPION-2), 2.5 g of T10 dextran was added. In following evaluations, the radioisotope in the NUSPIONs was ^{177}Lu unless otherwise noted.

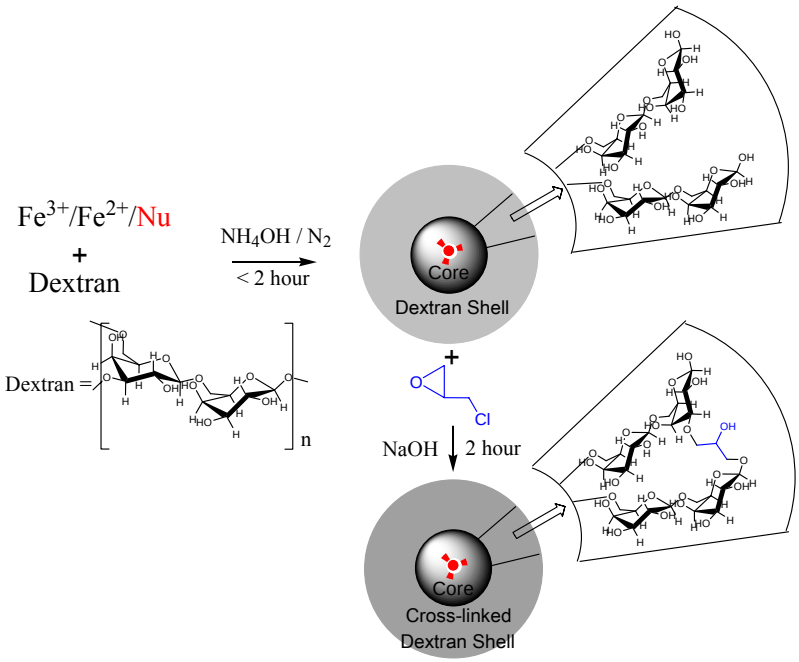

Figure 3. Synthetic scheme of NUSPIONs (NU: gamma- or positron emitting nuclides).

Conjugation of R11 with NUSPIONs

The purified and concentrated NUSPION-1 was reacted with 1 M chloroacetic acid in 3 M NaOH for 16 h at RT in order to introduce carboxylate groups to the dextran surface. The synthetic scheme of R11 conjugated NUSPIONs is shown in **Figure 4**. Unreacted chloroacetic acid was removed by three times of YM-100 centricon washing (3 × 2 mL), two of which were using 2 mL water while the last time using 2 mL of 50% DMSO solution in water. After the recovery of carboxylate functinalized nanoparticles in the DMSO solution (~ 600 μL), 22.5 mg of NHS and 9.2 mg of EDC in 100 μL of DMSO were added to produce activated NHS esters. Then 3 μL of 10 μg/μL of NH_2GR11 in DMSO was added to the reaction mixture, which was shaken at 650 rpm at RT for 3 h. The purification procedures were the same as above by using YM-100 centricon filters.

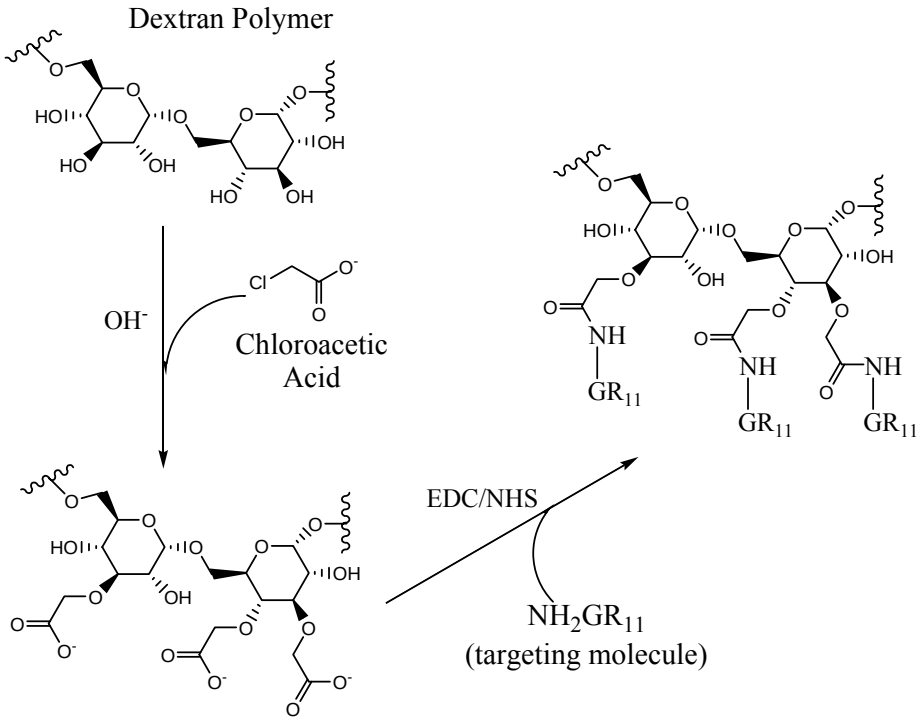

Figure 4. Scheme of NH_2GR11 conjugation with the surface dextran coating.

Characterization of CLIONPs or NUSPIONs

Particle size and size distribution

The hydrodynamic size (radius) and size distribution of the nanoparticles were measured by a Wyatt's DynaPro dynamic light scattering (DLS) system (Santa Barbara, CA). The sample was prepared by adding 60 μL of a diluted solution to a microCUVETTE, which was then loaded to the Wyatt's DynaPro DLS system. The sample was examined by adjusting the laser intensity to an appropriate range. The size was described as hydrodynamic radius (R_h).

Surface morphology of CLIONPs

The morphology and size of CLIONPs were examined by the FEI Tecnai G2 Spirit BioTWIN Microscope (TEM) system (Hillsboro, OR). Samples were prepared by transferring 2 μL of a diluted solution to a freshly glow discharged TEM copper grid (300 mesh copper Formvar/Carbon) and then allowed to dry at RT. The CLIONPs were also examined by Atomic Force Microscope (AFM) (NT-MDT SOLVER PRO, Moscow, Russia) before and after purification using a MICA substrate. The MICA samples were prepared by transferring 2 μL of a diluted solution to the freshly cleaved mica, under which a strong magnet was placed. The samples were allowed air dry.

Analytical chemistry of CLIONPs or NUSPIONs

Iron content measurement

The iron content of synthesized CLIONPs or NUSPIONs was measured by a colorimetric assay based on a reddish complex formation of KSCN with Fe^{3+} (*226*). Briefly, a series of Fe^{3+} standard dilutions (ranging from 0.10 to 1.50 mM) were prepared. To 500 μL of each standard Fe^{3+} solution, 100 μL of 0.1 M H_2O_2 and 400 μL of 0.26 M of KSCN were added. The colorimetric reaction was allowed to proceed for more than 1 h before the UV

absorbance was measured at 480 nm by a UV/Vis spectrometer (Milton Roy Spectronic 1201, Ontario, Canada). A standard linear calibration curve was generated by plotting the absorbance vales vs the iron concentrations.

Typically, a small portion of purified and concentrated nanoparticles were first diluted with water to an appropriate concentration (dilution factor I). To the 100 μL sample taken out from above diluted nanoparticle solution, 300 μL of concentrated HCl (12 N) was added to dissolve the iron oxide particles. Then 100 μL of 1 M H_2O_2 was added to convert Fe^{2+} into Fe^{3+}. The reaction was let go for 30 min and the final reaction mixture was then diluted with water to a proper volume (dilution factor II). Two portions of 500 μL of this hydrolyzed solution were taken out for the following colorimetric assay. To each portion of the 500 μL solution, 100 μL 0.1 M H_2O_2 and 400 μL of 0.26 M KSCN were added. Then the reaction mixture was mixed and incubated at RT for 1-2 h until the reading was stable. The UV absorbance was measured at 480 nm by the UV/Vis spectrometer. The concentration was calculated based on the standard calibration curve and the dilution factors.

Dextran content measurement

The dextran content was determined by the phenol-sulfuric acid color reaction (*227*, *228*). Dextran was first hydrolyzed to monomers by concentrated H_2SO_4, and then reacted with phenol to produce a dark reddish-colored product with a strong absorbance at 430 nm. Briefly, a series of standard dextran (T10) solutions (ranging from 0 to 1.0 mg/mL) were used to generate the calibration curve. To 500 μL of each dextran solution, 1 mL of 98% H_2SO_4 was added. The mixture was shaken for 30 min affording the complete hydrolysis of the dextran. To the hydrolyzed mixture, 200 μL of 0.88 M phenol solution was added. The reaction was allowed to proceed long enough (until the reading was stable) before the

absorbance was read at 430 nm by the UV/Vis spectrometer. A standard linear calibration curve was generated by plotting the absorbance vales vs the dextran concentrations.

Generally, a small portion of purified and concentrated nanoparticles were first diluted with water to an appropriate concentration (dilution factor). To the 100 μL sample taken out from above diluted nanoparticle solution, 400 μL water and 1 mL of 98% H_2SO_4 were added. After thorough mixing, the reaction mixture was sealed and kept shaking gently for 45 min. And then 200 μL of 0.88 M phenol solution was added. The reaction mixture was mixed and incubated for several hours until the reading was stable. The absorbance was read at 430 nm by the UV/Vis spectrometer. The concentration was calculated based on the standard calibration curve and the dilution factor.

In vitro evaluation

In vitro stability of CLIONPs or NUSPIONs

In vitro serum stability experiments were conducted by adding 20 μL of CLIONPs or NUSPIONs (with the iron concentration around 10 mM) to 180 μL of rat serum. The solutions were kept at RT, and sampled for the DLS assay at specific time points post-addition to rat serum. The stability of the particles in PBS (phosphate buffered saline) was assessed the same way by adding 20 μL of concentrated purified CLIONPs or NUSPIONs to 180 μL of 10 mM PBS. The hydrodynamic size of the sample was monitored over time for the stability evaluation.

In vitro magnetic resonance relaxivities of CLIONPs

In order to evaluate the potential of CLIONPs as MR contrast agents, a series of nanoparticle dilutions were used to determine the T_1 and T_2 relaxation times by a 4.7 T Varian MRI system (200 MHz ^{1}H) at 25 °C. A multicompartment phantom was used for

the relaxivity measurements where Fe concentrations were in the range 0.0-5.0 mM. For the T_1 and T_2 measurements, a spin-echo sequence was employed with varying echo times (TE) and recovery times (TR). Maps of the relaxation times T_1 and T_2 were computed on a voxel by voxel basis from least-squares fitting of the exponentially varying signals using the analysis routines available on the Varian MR system. Regions of interest (ROIs) were drawn on the maps around each compartment to obtain a mean relaxation rate for that concentration. Relaxivities were extracted from graphs of relaxation rates ($R_1 = 1/ T_1$ and $R_2 = 1/ T_2$, respectively) versus concentrations.

In vivo evaluation

HPLC and DLS analysis of NUSPIONs

The quality and purity of NUSPIONs was determined by HPLC (Waters 600 Multisolvent Delivery System equipped with a Waters 2996 Photodiode Array detector (Milford, MA), an in-line Shell Jr. 2000 radio-detector (Fredericksburg, VA) and Wyatt Mini DAWN light scattering detector (Santa Barbara, CA). Briefly, 20 μL (3-5 μCi) of NUSPIONs right after purification was injected into an Ultrahydrogel size exclusion column (separation range: 500-8×10^6 Da), which was eluted with 20 mM HEPES and 150 mM NaCl buffer at an isocratic flow rate of 1.0 mL/min. The acquisition by the light scattering detector was manually begun right after the injection. The radioactivity was monitored by either the inline radio-HPLC detector or gamma counting the fractions collected by the HPLC's fraction collector. The DLS was performed as described in the general characterization section.

Biodistribution in normal Balb/c mice

All animal studies were performed in compliance with guidelines set by the UT Southwestern Institutional Animal Care and Use Committee. The biodistribution of

NUSPIONs with two different sizes (NUSPION-1: R_h = 11.8 ± 1.3 nm and NUSPION-2: R_h = 30.6 ± 0.5 nm) were carried out in normal Balb/c mice. Each mouse was injected with 100 μL of NUSPIONs (~ 5 μCi) via the tail vein. The animals were anesthetized prior to sacrifice at each time point (1 h, 4 h, 24 h, and 48 h; n = 4). The animals of the last time point groups were housed in metabolic cages to collect urine and feces at 1 h, 4 h, 24 h and 48 h p.i. Organs of interest (blood, lungs, liver, spleen, kidneys, fat, muscle, heart, stomach, intestines and femur) were removed, weighed, and counted. Standards were prepared and counted along with the samples to calculate the percent injected dose per gram tissue (%ID/g) and percent injected dose per organ (%ID/organ). For the evaluation of pharmacokinetic parameters, 5-10 μL of blood was collected from the retroorbital sinus of the animals at 5 min, 10 min, 20 min and 30 min p.i. The parameters were calculated based on a two-compartment open model (*229*). The unpaired t-test on the biodistribution data was performed using Prism, v. 4.00 (Graphpad, San Diego, CA).

Biodistribution in PC-3 tumor-bearing mice

Sixteen PC-3 tumor-bearing mice were randomly separated into four groups and injected intravenously via the tail vein with 100 μL (~ 4 μCi) of NUSPION-1 or NUSPION-1-R11. Two time points (24 h and 48 h; n = 4) were chosen based on the results of biodistribution in normal mice. The mice were sacrificed at 24 h and 48 h p.i. The blood, lungs, liver, spleen, kidneys, fat, muscle, heart, stomach, intestines and tumors were harvested, weighed and the radioactivity was quantified. Standards were prepared and counted along with the samples.

Dual-modality imaging evaluation of NUSPIONs

The same tumor bearing animal model was used for the proof-of-concept dual modality imaging studies, in which both MRI and nuclear imaging were applied to the animals

injected with the dual-modality imaging agent (NUSPIONs). Because the incorporated radioisotope amount can be conveniently controlled in the preparation, we were able to inject the right amount of dose to enable the dual modality imaging studies. Specifically an injection dose of NUSPION-1 was prepared to contain 0.2 mmol/kg of iron, which is a typical SPIO dose for MRI scans and equivalent to a typical dose for mouse SPECT imaging (~ 100 μCi of ^{177}Lu-activity).

***In vivo* MR imaging**

Five PC-3 tumor-bearing mice were used for the MR imaging studies. When the tumors reached ~ 8 mm diameter, the animals were imaged under a 4.7 T magnet before and after the injection (1 h, 3 h and 48 h p.i.) of the CLIONP-1 (mean R_h = 10.2 nm) at a dose of 0.2 mmol/kg body wt Fe. Multi-slice T_2 maps were obtained using a spin echo sequence. ROI analysis was performed on a slice-by-slice basis using homebuilt Matlab routines. The T_2 values from all voxels of each tumor at each time point were pooled for statistical comparison by a t-test using Origin® program (OriginLab Corp., Northhampton, MA).

Prussian blue reaction for the iron stain of tumor slices post-MRI

The Prussian blue reaction involves the treatment of sections with the acid solution of ferrocyanides. The ferric ions (+3) present in the tissue react with ferrocyanide to form a bright blue pigment called Prussian blue, or ferric ferrocyanide (*230, 231*). Right after the MRI study, the tumors were excised and embedded in paraffin. After processing and embedding the tissue, slices with a thickness of 8 μm were cut by a Microm HM 315 microtome (Mikron Instruments, San Marcos, CA), and then baked on glass slides overnight in an oven at 40 °C. The sections were deparaffinized by xylene and xylene/ethanol (v/v: 1:1), and then hydrated by a series of ethanol solutions with descending contents of alcohol in deionized water prior to the staining. The hydrated

tissue section slides were immersed in a staining solution with equal parts of 2.40 M hydrochloric acid and 0.24 M potassium ferrocyanide for 20 min, and then removed from the solution and rinsed 3 times with deionized water. The slides were further counterstained with Nuclear Fast Red solution for 5 min and rinsed two portions of deionized water. To visualize the iron stains, a cover slip was fastened to each of the slides using Permount Mounting Medium (Fisher Scientific, Houston, TX) after the sections were dehydrated through ethanol solutions in deionized water with ascending contents of alcohol to 100% xylene. The presence of iron is shown as bright blue spots while the nuclei of cells red and the cytoplasm pink.

***In vivo* autoradiography**

Autoradiography was performed on a PerkinElmer Cyclone storage phosphor system with OptiQuant software (Waltham, MA). Three PC-3 tumor-bearing mice were used for autoradiography imaging of each NUSPION. The PC-3 tumor-bearing mice were injected intravenously via the tail vein with ~ 110 μCi of NUSPION-1 or NUSPION-2. The mice were anesthetized by a mouse cocktail (Ketamine 30 mg/ml + Xylazine 4 mg/ml) 5 min before each time point (1 h, 4 h, 24 h, 48 h and 72 h p.i.). The exposure time was 60-90 seconds.

Post-autoradiography biodistribution study

Right after the 72 h p.i. autoradiography, the animals were sacrificed. Organs of interest (blood, lungs, liver, spleen, kidneys, fat, muscle, heart, stomach, intestine, femur and brain) were removed, weighed, and counted. Standards were prepared and counted along with the samples to calculate the percent injected dose per gram tissue (%ID/g) and percent injected dose per organ (%ID/organ).

CHAPTER 3 RESULTS AND DISCUSSION

Radiolabeling and Biodistribution of DOTA-R11

DOTA-R11 was successfully labeled with ^{64}Cu by incubating with $^{64}CuCl_2$ in 0.1 M NH_4OAc buffer (pH = 6.5) at RT for 1 h. The radio-TLC results demonstrated that the DOTA-R11 was effectively labeled with ^{64}Cu with radiochemical yield of near 100%. The purification via C-18 Sepak Cartridge afforded nearly 100% radiochemical purity for ^{64}Cu-DOTA-R11 as determined by radio-HPLC. The highest specific activity of ^{64}Cu-DOTA-R11 achieved was ~ 650 μCi/nmol.

The biodistribution studies of ^{64}Cu-DOTA-R11 in normal mice, PC-3 or T-24 tumor-bearing mice were conducted for the *in vivo* evaluation and the verification of the preferential accumulation of R11 in prostate or bladder. The tissue distribution data are presented in **Figures** 5-6. Indeed ^{64}Cu-DOTA-R11 demonstrates a strong tendency to accumulate in prostate and bladder in both normal and tumor-bearing mice. However, the large standard deviations may be likely representing animal individual difference. The other major organs such as blood, lungs, spleen, bone and muscle showed very low uptake. These biodistribution results are consistent with the previous studies using FITC tagged R11 in the same animal model. It indicates that R11 may have the potential for prostate or bladder cancer targeting. The pharmacokinetics of ^{64}Cu-DOTA-R11 was also evaluated by using a two-compartment model. Its half-life in the blood (the primary compartment) was about 10.7 min; and the elimination half life from other organs (the secondary compartment) was 17.2 h.

Based on these observations, R11 was selected to conjugate with our NUSPIONs for prostate cancer targeting. By conjugating R11 with NUSPIONs, we anticipate that the nano-conjugates could have significantly enhanced prostate-specific binding resulted

from the multi-presentation of R11 on the nanoparticle surface and the facilitation of cellular internalization by R11. Furthermore, we expected the pharmacokinetic properties of nanoparticles could be optimized by conjugating with R11.

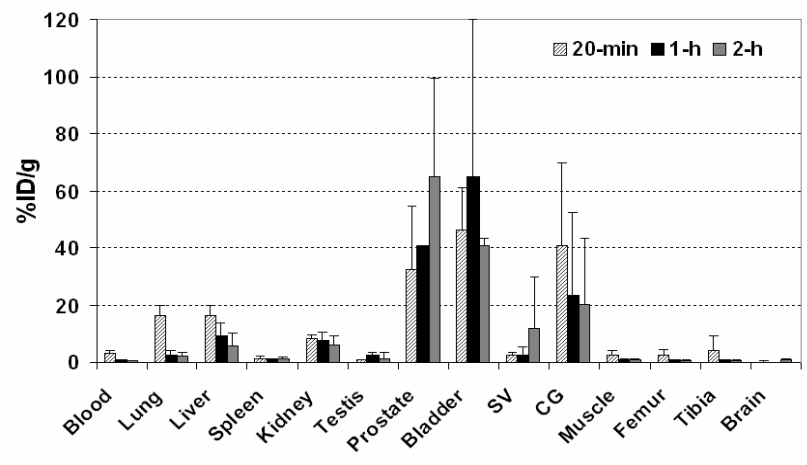

Figure 5. Biodistribution of ^{64}Cu-DOTA-R11 in normal nude mice (n = 4). Data are presented as %ID/g ± s.d.

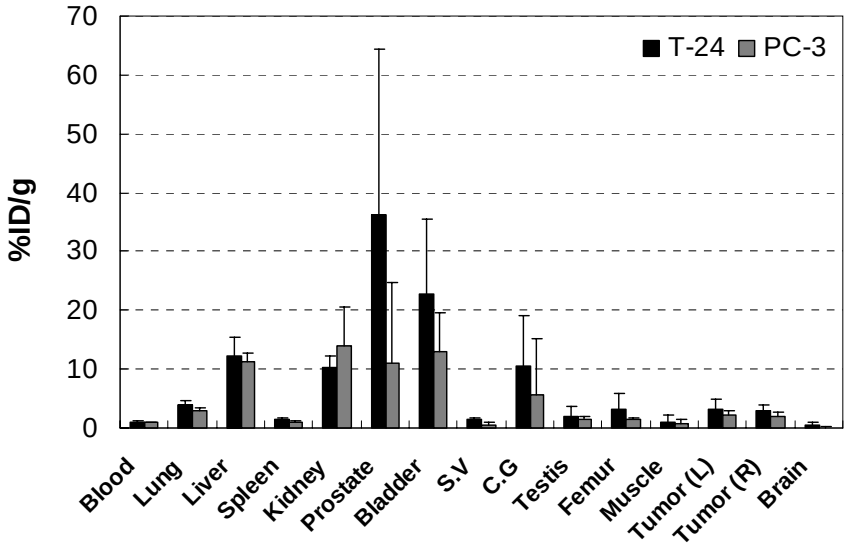

Figure 6. Biodistribution of ^{64}Cu-DOTA-R11 in PC-3 and T-24 tumor-bearing mice (n = 4) at 1 h p.i. Data are presented as %ID/g ± s.d.

Nanoparticle synthesis and characterization

Determinants of the size and size distribution

In the early trials, a dextran (MW 64-76 KDa) purchased from Sigma-Aldrich was used for the preparation of nanoparticles. When using large excess amounts of dextran, factors such as concentration, temperature, and incubation time were evaluated for their roles in the controlling of nanoparticle size and size distribution. Among them, only the concentrations of Fe^{3+} and Fe^{2+} significantly affect the final particle size (Tables 4-6). As shown in Table 4, the particle size decreases with the concentration decreasing of Fe^{3+} and Fe^{2+}. Based on the optimal conditions found when using the 64-76 KDa dextran, the FDA approved T10 dextran (MW 10 KDa) was used later instead to prepare nanoparticles with more uniform size for biological evaluations. Interestingly we found out that within a certain concentration range (shown in Table 7) of the dextran, the nanoparticle size is dependent on the amount of dextran T10 added when the Fe^{3+} and Fe^{2+}concentrations are fixed. Compared with the 64-76 KDa dextran-coated nanoparticles, dextran T10-coated nanoparticles indeed are more uniform and their sizes can be better controlled and reproduced. For example, when comparing the size distribution of the nanoparticles coated with these two different dextrans in the R_h range of 10-30 nm, the size distribution of T10-coated nanoparticles is as narrow as 11.8 ± 1.3 nm and 30.6 ± 0.5 nm while that of the 64-76 KDa dextran-coated nanoparticles is 12.9 ± 5.54 nm and 28.6 ± 4.6 nm respectively.

Table 4. Particle size (R_h) vs iron concentrations

[Fe^{2+}] (mM)	34.0	9.60	3.26	2.07	1.85	0.20
[Fe^{3+}] (mM)	35.0	4.90	2.82	2.01	1.81	0.19
Size (nm)	28.6 ± 4.6	20.5 ± 9.7	14.6 ± 7.6	19.7 ± 4.4	12.9 ± 5.5	7.49 ± 2.6

Table 5. Particle size (R_h) vs reaction temperature

Temperature	25 °C	53 °C	60 °C	85 °C
Fe^{2+}/Fe^{3+} (mM)	4.90/5.78	4.90/5.78	2.51/3.01	2.51/3.01
Size (nm)	20.5 ± 9.70	21.6 ±7.71	29.4 ± 15.1	31.1 ± 12.4

Table 6. Particle size (R_h) vs reaction time

Incubation time (h)	1 h	2 h	3 h	4 h
Size (nm)	24.9 ± 8.44	31.1 ± 12.4	22.8 ± 10.4	23.3 ± 10.1

Table 7. Particle size (R_h) vs T10 dextran added when the iron concentration is fixed

T10 dextran (mg)	300	500	850	1000
Size (nm)	128.7; 32.6	41.2	11.4	5.7
Notes	Two species Broad distribution	Broad distribution	Narrow distribution	Narrow distribution

Nanoparticle characterization by DLS, AFM and TEM

DLS is a routine and important characterization method to examine the hydrodynamic size and size distribution of the nanoparticles. By careful control of synthesis conditions, T10 dextran indeed affords more uniform nanoparticles than 64-76 KDa dextran. Here in **Figure 7** shows some DLS data of CLIONPs with similar size by using T10 or 64-76 KDa dextrans respectively.

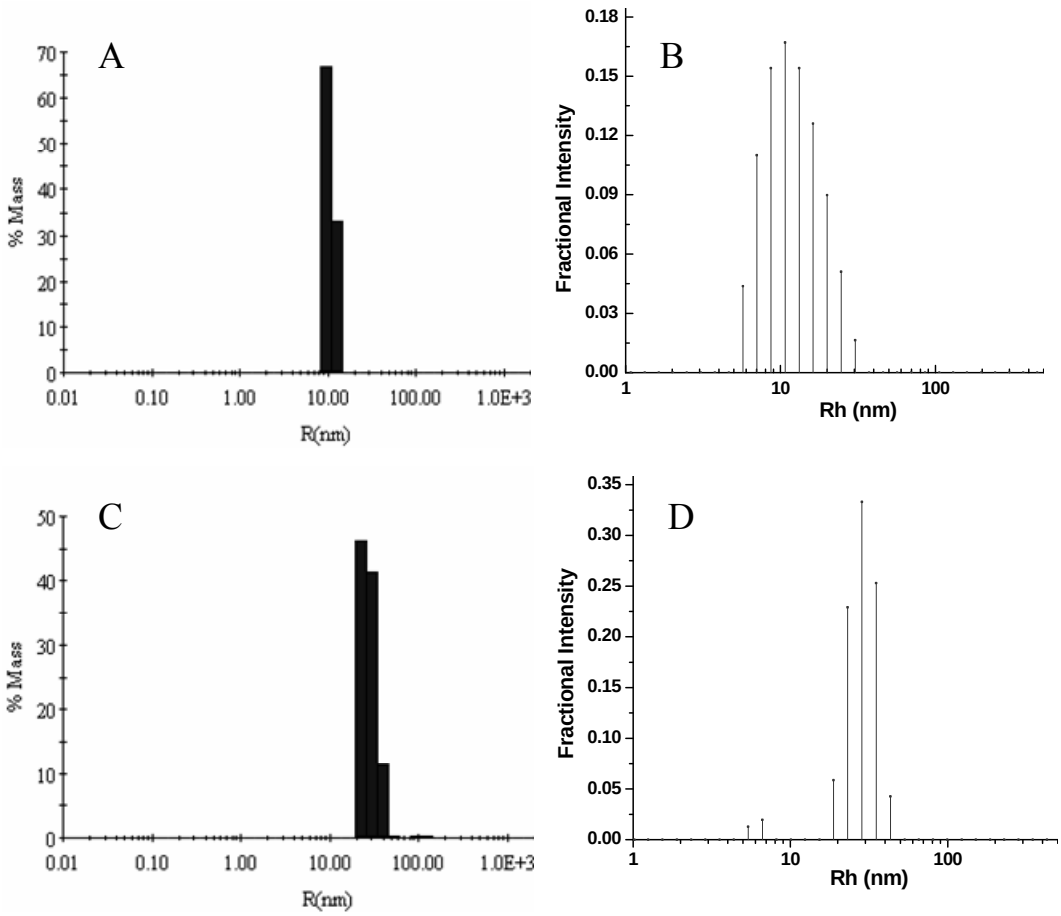

Figure 7. DLS results of CLIONPs coated with T10 dextran: (A) mean R_h = 10.8 nm and (C) mean R_h = 28.6 nm or 64-76 KDa dextran: (B) mean R_h = 12.9 nm and (D) mean R_h = 29.1 nm.

As one of the best tools to visualize nanoscale objects, the highly sensitive AFM instrument has been designed to measure the small attractive and repulsive forces that a sharp tip experiences when it is brought near to or in contact with a surface (*232*). Besides providing a true three-dimensional surface profile, most AFM modes can work perfectly well in ambient air or even a liquid environment, retaining the original properties of samples. Therefore, unlike TEM or SEM, AFM can also provide the hydrodynamic information of nanoparticles. Shown in **Figure 8** are representative AFM images of iron oxide nanoparticles coated with the 64-76 KDa dextran. The samples before and after purification via centricon filter washing were examined by AFM under

the same condition. It is clear that before purification, there was a small MW species on the MICA substrate (**Figure 8 A**). After purification, the samples exhibit a shape image with a clean background, demonstrating that centricon filter washing can efficiently remove small molecular species from the nanoparticles. Since the surface of MICA substrate is hydrophilic, the nanoparticles with a hydrophilic surface coating can be well dispersed on the substrate. Neither aggregates nor clusters are observed from the images. However, the hydrophilic dextran coating of the nanoparticles may stretch over the hydrophilic MICA substrate, resulting in the non-spherical morphology of the nanoparticles observed from the 3D image.

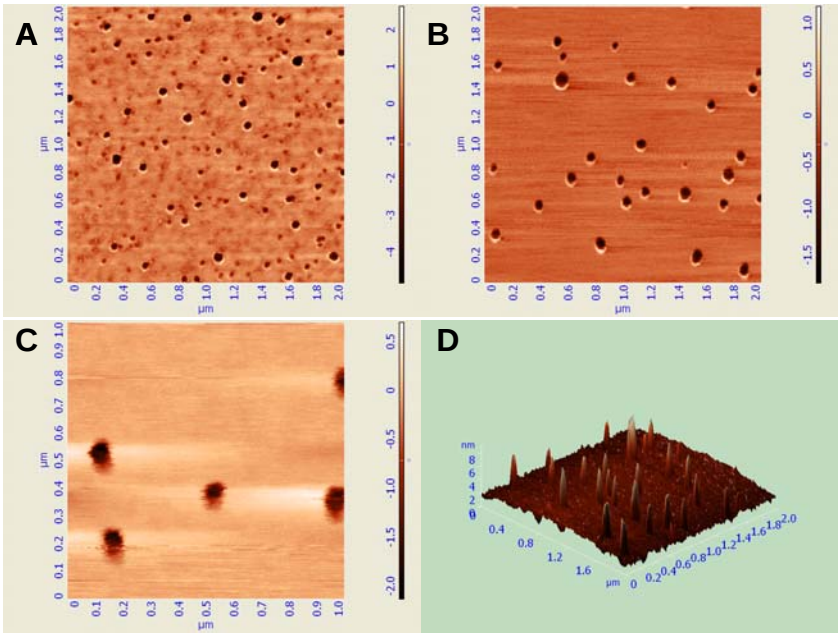

Figure 8. AFM images of iron oxide nanoparticles coated with the 64-76 KDa dextran on a MICA substrate before (A) and after (B, C) purification, and (D) the corresponding 3D image of the purified sample from B.

Shown in **Figure 9** are TEM images of the two distinct nanoparticles (CLIONP-1 and CLIONP-2). Because DLS provides information on the hydrodynamic particle size of the whole particles including the dextran coating layer and the SPIO core, while the TEM examines only the size of the SPIO core. Based on the size information obtained from

DLS and TEM, the dextran shell of CLIONP-1 is calculated to be about 5 nm thick and that of CLIONP-2 about 20 nm thick.

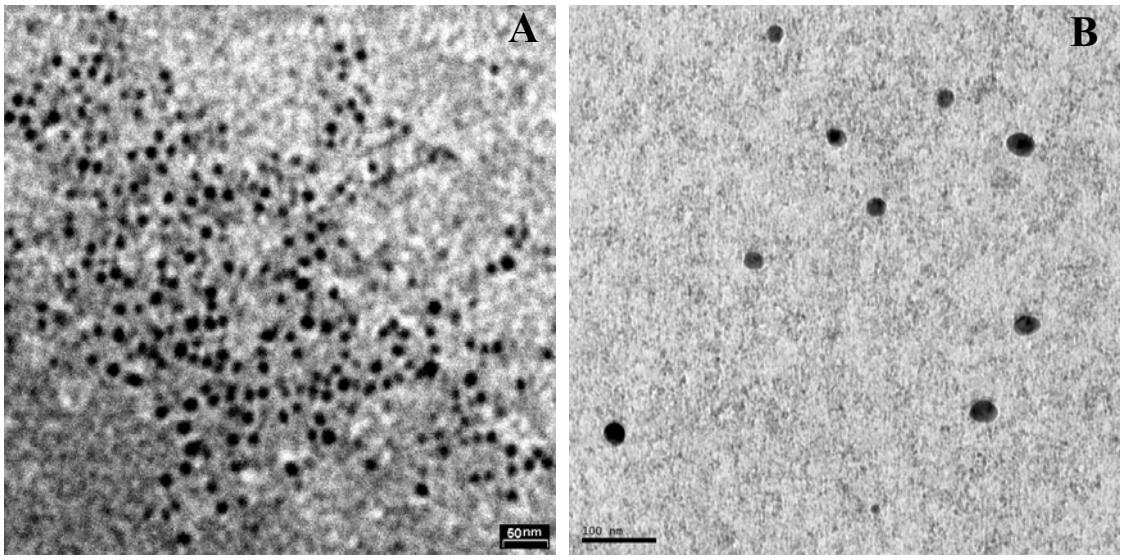

Figure 9. TEM micrographs of synthesized CLIONPs (A) CLIONP-1, scale bar 50 nm and (B) CLIONP-2, scale bar 100 nm.

Analytical chemistry of CLIONPs or NUSPIONs

The determination of iron and dextran concentration was examined by Ferric thiocyanate colorimetric assay and Phenol-sulfuric acid colorimetric reaction respectively. Firstly, the standard calibration curves were generated based on known concentrations. A strong linear regression calibration curve ($r^2 > 0.98$) was obtained by plotting the absorbance vales vs the iron concentrations or the dextran concentrations (**Figure10**). The iron or dextran content of the nanoparticles can then be deducted from the standard calibration curves.

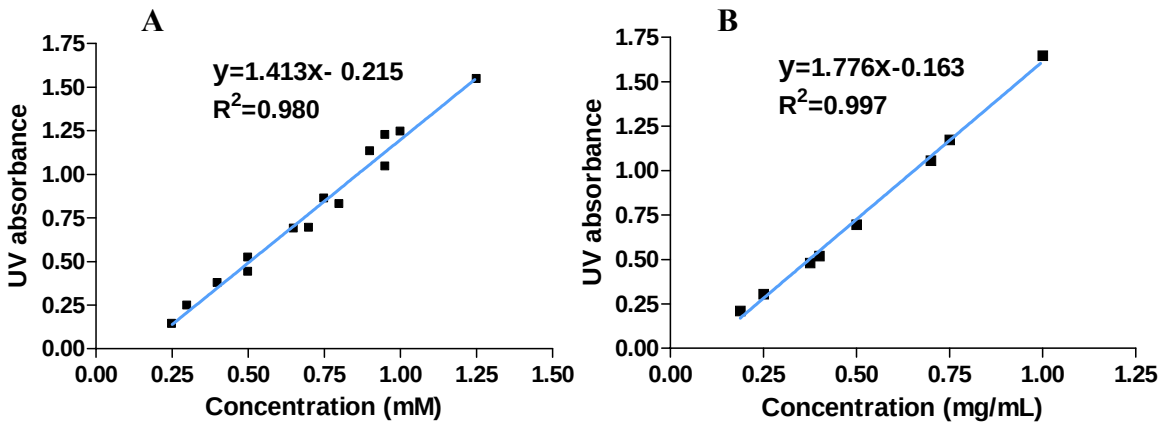

Figure 10. Standard calibration curves of (A) iron content and (B) dextran content.

Preparation of NUSPIONs

The efficient incorporation of a radioisotope into the nanoparticle core depends mostly on the characteristics of the radionuclide itself and the method of its incorporation. When selecting appropriate radioisotopes, it must take into consideration the physical half-life, the photon or particle energy of the radionuclide and its selective deposition of energy in tissues, the method of labeling (covalent binding, chelation or coprecipitation), and the effect that the chemical changes inherent in the labeling process may have on the properties of the nanoparticles.

Most importantly, the rate of radionuclide decay must be balanced with the rate of biolocalization of the nano-conjugates along with clearance of radioactivity from normal tissues. To be compatible with the long biological half-lives of nanoparticles (typically over one day), longer physical half-life emitters are needed for the exploration of nanoparticle biomedical applications. An additional reason to choose the radioisotopes with reasonably long half-lives is that it allows us to carry out the preparation, characterization, and *in vitro* / *in vivo* evaluation of the nanoparticles.

The availability and the properties of particular radioisotopes are often the limiting

factors in designing an imaging or therapy methodology. When the intended use is diagnostic, then what is required is high-photon density to achieve the high resolution and sensitivity (ideally no beta or alpha decay), whereas the therapeutic use requires radionuclides with high energy deposition at the target sites, i.e. beta or alpha emitters. For SPECT imaging, the energies of γ photons need to be in the energy window of NaI detector (e.g., ^{99m}Tc decays by 140 keV photons, which is ideal) while for PET imaging, higher abundance and lower energy of β^+ is desirable (e.g., ^{18}F, which has 97% β^+ abundance with $E_{\beta+}$ of 635 keV).

In this project, four isotopes (^{111}In, ^{177}Lu, ^{64}Cu and ^{74}As) were chosen for the NUSPION preparation, all of which can be practically doped into the iron oxide core via the coprecipitation with ferric or ferrous under specific conditions. Indium-111 has an appropriate half-life (2.8 days) and γ-emission characteristics (171 and 245 keV) for SPECT imaging. Lutetium-177 has a physical half-life of 6.7; it emits β particles (E_{avg} 133 KeV) that can be used for therapy and two relatively low energy gamma rays (113 and 208 keV) that allow SPECT imaging. Copper-64, a commonly used PET isotope, has shown great potential in PET imaging and radiotherapy due to its desirable decay characteristics ($t_{1/2}$ = 12.7 h; β^+: 0.653 MeV, 17.4%; β^-: 0.578 MeV; 39%) and its production in high yield and specific activity on a biomedical cyclotrons. The half life of ^{64}Cu is long enough for the synthesis of many radiopharmaceuticals, and compatible with the biological kinetics of a variety of large and small molecular carriers (*233-235*). Arsenic-74 was chosen for this project because it has a lower endpoint positron energy (0.94 MeV β^+) than that of three of the four conventional PET isotopes (^{11}C: 0.96 MeV β^+; ^{13}N: 1.19 MeV β^+; ^{15}O: 1.72 MeV β^+; ^{18}F: 0.64 MeV β^+). An isotope emitting higher energy positron results in lower PET resolution and gives an additional radiation dose to

patients.

We have established the standard operation procedures for the synthesis of NUSPIONs and the following surface functionalization. The incorporation of radioisotopes was achieved by the coprecipitation of radioisotopes with ferric and ferrous salts from their aqueous solution by the addition of ammonia. In the procedures, we adopted a size-exclusion centrifugation technique to expedite the separation and purification of nanoparticles, which typically took less than 5 h rather than over days if using dialysis tubes or lengthy column separation as in the preparation of SPIO. All these four radioisotopes were successfully incorporated (Table 8), among them, ^{177}Lu showed the highest incorporation efficiency at 74%. Although ^{64}Cu has a relatively short half life, the incorporation of ^{64}Cu could be accomplished using our developed approach in 2 h with an incorporation rate of 72%. The preparation methods are reliable and the results are reproducible.

Table 8. Incorporation rate of different radioisotopes into nanoparticles

Radioisotopes	**Half-life ($t_{1/2}$)**	**Incorporation rate**
Indium -111	2.8 d	69 ± 2%
Lutetium -177	6.7 d	74 ± 3%
Copper -64	12.7 h	72 ± 2%
***Arsenic -77**	38.8 h	58.0%

***** Arsenic -77 was used instead of ^{74}As due to the high cost of ^{74}As.

The multifunctional nanoscaffolds prepared by incorporating gamma- or positron-emitting radioisotope to the SPIO core are intended to enable the dual modality (MR/nuclear) imaging combining the excellent resolution and superior sensitivity. There are several advantages of our approach. First, it preserves the intact nanoparticles surface

for further surface modification or functionalization; Second, the radiotracer sits in the nanoparticle core, which avoids the *in vivo* transchelation of radiometals; therefore it guarantees the integrity of the dual-modality imaging probes *in vivo*; Third, the radiation therapy can be achieved by simply adjusting the loading amount of radioisotopes to the nanoparticle core.

At the beginning of this project, Dr. Sun obtained a DOE sponsored Reactor Sharing award from the University of Missouri at Columbia for the supplies of ^{177}Lu. Therefore ^{177}Lu-doped nanoparticles were used for the following *in vitro* and *in vivo* evaluation unless otherwise noted.

Preparation of two distinct nanoparticles

The size of nanoparticles plays a critical role in their biological activities. Generally, the size of the particles must be large enough to inhibit their leakage into the blood capillaries (*236*), but the phagocytotic activity increases with size of particles (*237*). Therefore, we plan to control the size (R_h) of nanoparticles in range of 10-30 nm to achieve optimal biological behavior of nanoparticles (long blood circulating time and low RES accumulation). In this thesis, two distinct iron oxide nanoparticles with different sizes, namely CLIONP-1 or NUSPION-1 with a mean R_h of 11 ± 2 nm and CLIONP-2 or NUSPION-2 with a mean R_h of 28 ± 3 nm, were synthesized, characterized and evaluated *in vitro* and *in vivo*.

When the concentrations of ferric and ferrous salts were fixed, the only determinant for synthesis of these two distinct particles was the T10 dextran amount added. The smaller nanoparticles were prepared by addition 5.0 g of dextran T10, while the larger ones were prepared by addition of 2.5 g of dextran T10. The incorporation of radioisotopes was achieved by their simultaneous precipitation with the iron salts. The incorporation of

radioisotopes does not affect the final size and size distribution.

Surface functionalization for active targeting

For biomedical applications, surface functionalization of iron oxide nanoparticles is essential in order to afford the stealthyness of the RES uptake, reasonably long blood circulation, and specific targeting. The size as well as the surface properties of the nanoparticles is the crucial factor for practical *in vivo* study. It is advantageous to have a hydrophilic surface from the biocompatibility point of view, which can minimize opsonization and subsequent clearance by the macrophage. Surface conjugation with ligands such as antibodies, peptides, aptamers or small organic molecules can be achieved by either physical adsorption or covalent chemical bonds to the nanoparticle surface. But covalent surface modification is generally favored over physical adsorption because it renders superior stability (*238-240*).

Previous screen studies of CPPs for optimal intracellular delivery of a proline-rich domain for prostate cancer therapy showed that R11 accumulated preferentially in prostate and bladder tissues. Our *in vivo* biodistribution studies demonstrated the strong tendency of ^{64}Cu-DOTA-R11 to accumulate in prostate and bladder. Therefore R11 was chosen to conjugate with NUSPIONs for prostate cancer targeting.

DLS and radio-HPLC analysis

After the purification, the two distinct NUSPIONs with different sizes were examined by DSL and HPLC. As shown in **Figure 11,** NUSPION-1 had a R_h of 11.8 ± 1.3 nm, with over 97.2% in mass% while NUSPION-2 had a R_h of 30.6 ± 0.5 nm, with over 96.3% in mass%. The incorporation of radioisotopes did not affect the nanoparticle size. After R11 conjugation, the size was increased from 11.8 nm of NUSPION-1 to 19.2 nm with over 96.2% in mass% of NUSPION-1-R11, which probably caused by the aggregation resulted

from the destroy of the surface dextran coating during the long duration (> 10 h) of reaction under harsh condition (3 or 5 M NaOH).

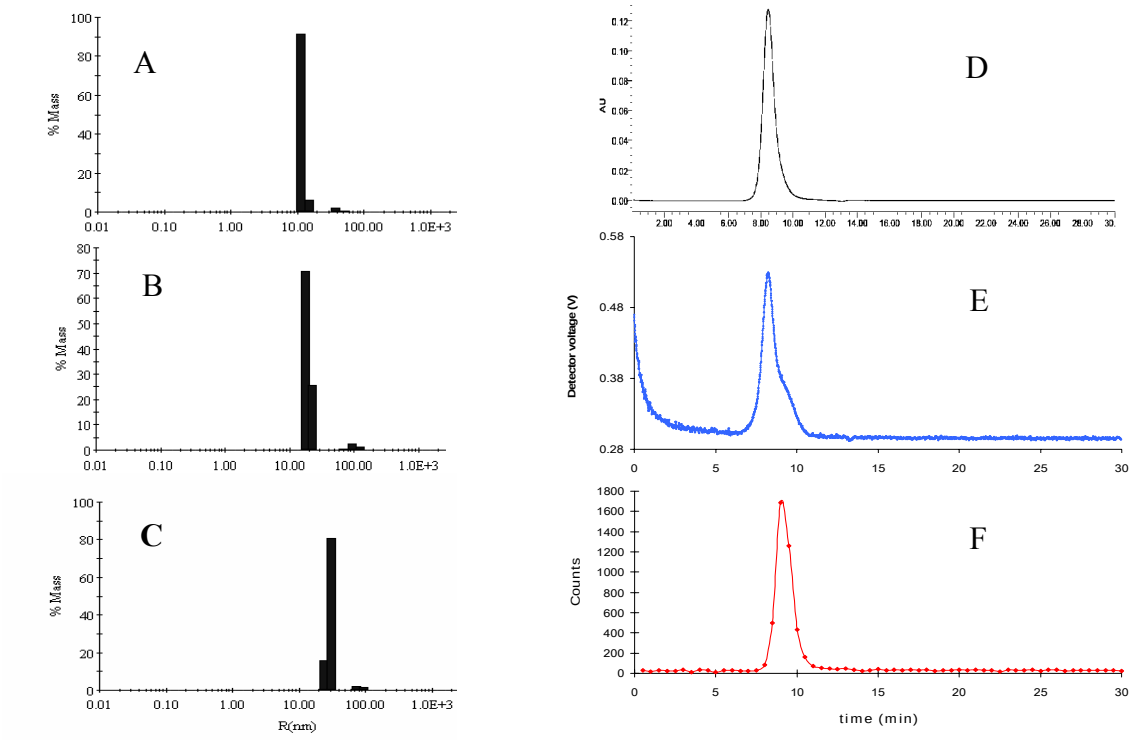

Figure 11. DLS and HPLC analysis. DLS data of (A) NUSPION-1 with a mean Rh of 11.8 nm, (B) after R11 conjugation, NUSPION-1-R11 with a mean R_h of 19.2 nm, and (C) NUSPION-2 with a mean R_h of 30.6 nm; and HPLC (only NUSPION-1 is shown here (D) signal from UV detector at 254 nm, (E) signal from light scattering detector and (F) signal plotted from fractions counted via gamma counter.

The integrity of NUSPIONs is critically important for their applications. Therefore we have developed a sensitive and reliable method by using an HPLC system equipped with three different detectors: a Wyatt Mini DAWN light scattering detector for the nanoparticles, a Waters UV2996 PDA for a wide range of UV detection of functional molecules anchored on the surface of NUSPIONs as well as the particles themselves, and an HPLC radiodetector for the radioisotopes. Shown in **Figure 11** (D, E and F) is a typical stack display of the HPLC spectra acquired from the three detectors. By the three HPLC readouts, we can convincingly and accurately determine the integrity of

NUSPION-based multifunctional probes (all functional components are present in the same nanoscaffold) and their *in vitro* and *in vivo* stability. In addition, this HPLC method can be used to monitor the conjugation reactions and the separation/purification procedures. It is noteworthy that the UV peak intensity (area) change at a certain wavelength before and after a molecule conjugation can be used to quantify the number of the molecule that have been linked to the nanoparticle surface.

In vitro stability study of CLIONPs or NUSPIONs

The CLIONPs or NUSPIONs stayed > 92% intact in rat serum while a small portion of nanoparticles aggregated, and > 99% in 10 mM PBS out to 72 h. The high *in vitro* stability exhibited by the nanoparticles warrants their further *in vivo* evaluation.

In vitro magnetic resonance relaxivities of CLIONPs

In order to evaluate the potential of CLIONPs as MR contrast agents, magnetic properties were examined by a 4.7 T Varian MRI system at 25 °C. The T_1 and T_2 maps of a phantom containing different concentrations of the CLIONP-1 are shown in **Figure 12**. In **Figure 13**, the relaxation rates (R_1 = 1/ T_1 and R_2 = 1/ T_2) are shown as a function of the nanoparticle concentrations, both of which show a perfect linear relationship ($r^2 > 0.99$). The relaxivities, r_1 and r_2, representing the slopes of these curves, were calculated to be 0.31 and 15.19 $s^{-1}mM^{-1}$, respectively.

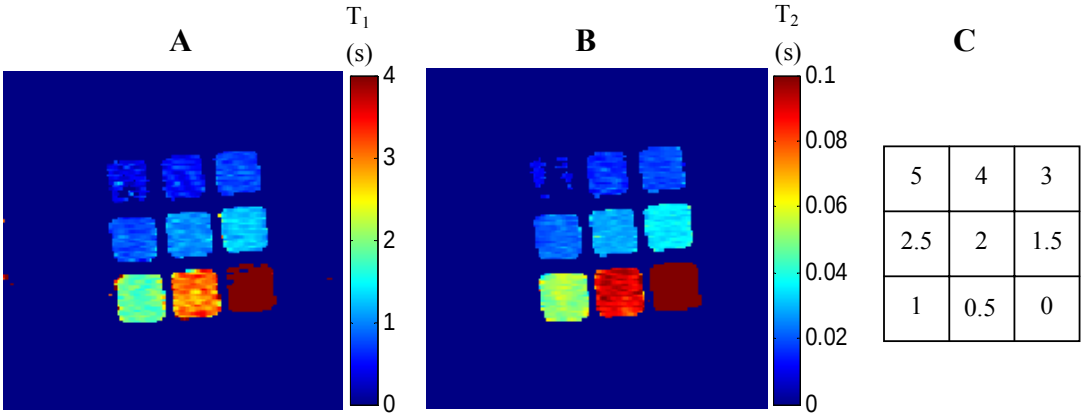

Figure 12. *In vitro* magnetic resonance relaxivities of CLIONP-1. (A) T_1 and (B) T_2 maps of the phantom containing different concentrations of the CLIONP-1, (C) Schematic loading of sample vials containing CLIONP-1 (in mM) in the phantom. "0 mM" refers to deionized H_2O.

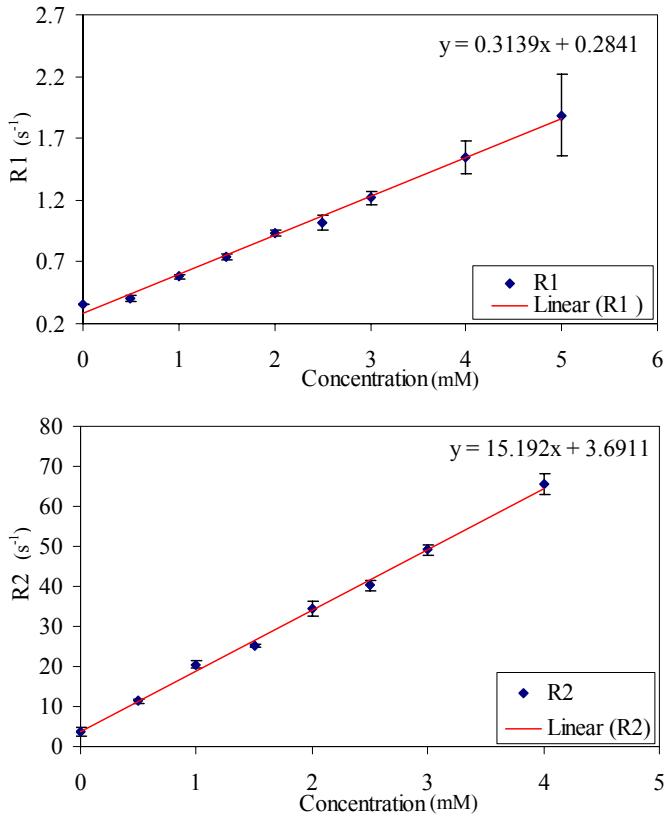

Figure 13. Proton relaxivities, R_1 and R_2 of CLIONP-1 at 4.7 T, 25 °C.

Summarized in Table 9 are the MR relaxivities of T10-coated iron oxide nanoparticles with a mean R_h of 11 ± 2 nm measured at different temperatures, 64-76 KDa-coated iron oxide nanoparticles with a mean R_h of 12 nm and a commercial iron oxide nanoparticles

(Ferumoxtran-10 AMI-227) adapted from other's report for comparison (*76*). All the transversal relaxivity r_2 was found to be significantly higher than longitudinal r_1, confirming the efficiency of these nanoparticles as T_2 contrast agents. MR contrast results from the difference between r_1 and r_2 values. In the case of T_2 contrast agents, the higher the r_2-to-r_1 ratio is, the better the agent's effectiveness is (*241*). Compared with Ferumoxtran-10 AMI-227, our nanoparticles showed much smaller r_2 values probably due to the size difference or magnetic field strength difference, but significantly higher r_2-to-r_1 ratio. It is apparent that the 64-76 KDa dextran-coated nanoparticle showed a higher r_2 value than the T10-coated one likely due to the size difference or the different dextran coating. The temperature seems to affect the relaxivities at some degree. The lower the temperature is, the higher the r_2 is. In summary, our T10-coated iron oxide nanoparticles are the best in terms of contrast effectiveness and have demonstrated their promising potential to be used as T_2 contrast agents.

Table 9. Magnetic Resonance relaxivities (r_1 and r_2) measured at 4.7 T (200 MHz)

Sample	Measurement Temperature (°C)	Longitudinal relaxivity (r_1) $mM^{-1}s^{-1}$	Transverse relaxivity (r_2) $mM^{-1}s^{-1}$	r_2/r_1
CLIONP-1 (a)	25	0.30	15.2	49.0
T10 dextran-coated (b)	18	0.64 ± 0.04	18.8 ± 1.9	29.4
	25	0.64 ± 0.04	13.6 ± 0.4	21.3
	37	0.85 ± 0.04	13.2 ± 1.2	15.5
64-76 KDa dextran-coated (c)	37	1.67 ± 0.07	29.0 ± 0.4	17.4
AMI-227(Sinerm) (d)	37 (at 1.5 T)	9.9	65.0	6.6

(a) The same sample used for both the *in vitro* and *in vivo* evaluation described in this thesis; (b) MR relaxivities measurement of T10 dextran-coated iron oxide nanoparticles with the equivalent size of CLIONP-1 (mean R_h = 11 ± 2 nm); (c) 64-76 KDa dextran-coated iron oxide nanoparticles (mean R_h = 12 nm); (d) The commercial T10-coated oxide nanoparticles (R_h: 7.5-15 nm).

In vivo evaluation of NUSPIONs or CLIONPs

Table 10 lists the injection dose information for the following *in vivo* evaluation. The iron content of injection doses were measured and calculated based on the standard calibration curves generated. The preparation of injection dose for biodistribution is normally based on the radioactivity. The large variation of iron concentration for the injection doses between the biodistribution in normal mice and tumor-bearing mice results mainly from the amount of radioactivity and the specific activity of the radioisotopes added when preparing the nanoparticles.

Table 10. Injection doses for the *in vivo* evaluation

Studies	Compound	Activity μCi	Iron content mmole/kg (Fe)
Biodistribution in normal mice	NUSPION-1	~ 5 μCi	0.053
	NUSPION-2	~ 5 μCi	0.041
Biodistribution in PC-3 tumor-bearing mice	NUSPION-1	~ 4 μCi	0.012
	NUSPION-1-R11	~ 4 μCi	0.073
MRI	CLIONP-1		0.20
Autoradiography imaging	NUSPION-1	~ 110 μCi	0.17
	NUSPION-2	~ 110 μCi	0.15

Biodistribution in normal Balb/c mice

In order to evaluate how the particle size affects the biological behavior of the nanoparticles in living animals, two distinct NUSPIONs (NUSPION-1: R_h = 11.8 ± 1.3 nm; NUSPION-2: R_h = 30.6 ± 0.5 nm) were used for the biodistribution study in normal mice. The biodistribution results of NUSPIONs are presented in Tables 11, 12 and **Figure 14**. The time activity curves of the two NUSPIONs in major organs (blood, liver, spleen, kidney, lung, and muscle) are compared in **Figure 15**. As expected, both NUSPIONs showed high accumulation and long retention in liver and spleen, the major RES organs.

At early time points (1 h and 4 h p.i.), compared with NUSPION-2, NUSPION-1 showed significantly higher ($p < 0.0001$) blood uptake, and even up to twenty times higher at 4 h p.i. (NUSPION-1: 39.29 ± 0.84 %ID/g at 1 h p.i. and 23.29 ± 1.99 %ID/g at 4 h p.i.; NUSPION-2: 5.34 ± 0.38 %ID/g at 1 h p.i. and 1.11 ± 0.12 %ID/g at 4 h p.i.), and significantly lower uptake in liver (9.24 ± 1.12 %ID/g vs 43.45 ± 3.55 %ID/g at 1 h p.i., $p < 0.0001$; and 18.41 ± 0.58 %ID/g vs 32.80 ± 3.88 %ID/g at 4 h p.i., $p = 0.0003$) and spleen (5.83 ± 0.36 %ID/g vs 30.05 ± 1.36 %ID/g at 1 h p.i., $p < 0.0001$; and 12.61 ± 2.19 %ID/g vs 20.20 ± 4.85 %ID/g at 4 h p.i., $p < 0.05$). Bone also showed high uptake and long retention. This is likely due to the macrophage expression in the bone marrow. No significant fat, muscle, heart, intestines and stomach uptake was observed for either of the NUSPIONs.

Knowledge of quantitative biodistribution of these nanoparticles is of paramount importance for any diagnostic or therapeutic application in living animals. It can be concluded from the biodistribution studies of these two distinct nanoparticles in normal mice that the nanoparticle size affects the tissue distribution and blood clearance greatly. The smaller nanoparticles (NUSPION-1) showed desirable tissue distribution profile (much higher uptake and longer retention in blood which is good for both imaging and therapy, and less liver and spleen uptake). Therefore it was chosen for the further evaluation in a prostate tumor xenograft mouse model.

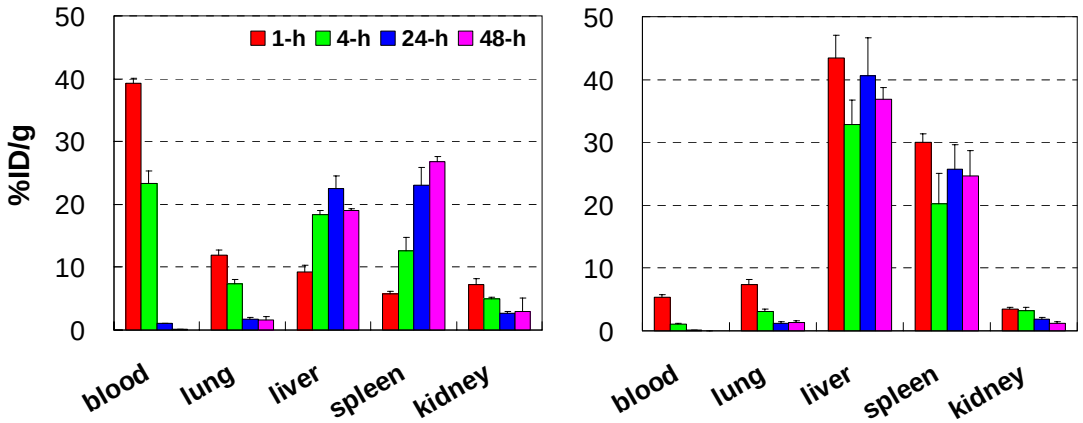

Figure 14. Biodistribution of NUSPIONs in normal mice. (A) NUSPION-1 and (B) NUSPION-2. Data are presented as measured radioactivity in blood, lung, liver, spleen and kidney (%ID/organ ± s.d., n = 4).

Table 11. The biodistribution of NUSPION-1 in normal Balb/c mice (n = 4). Data are presented as %ID/g ± s.d. and %ID/organ ± s.d.

organ	%ID/g				%ID/organ			
	1 h	4 h	24 h	48 h	1 h	4 h	24 h	48 h
blood	39.29 ± 0.84	23.29± 1.99	1.06 ± 0.02	0.12 ± 0.03	57.53 ± 0.29	37.18 ± 3.01	1.52 ± 0.03	0.18 ± 0.05
lung	11.93 ± 0.82	7.44 ± 0.62	1.73 ± 0.31	1.59 ± 0.55	1.56 ± 0.20	1.09 ± 0.16	0.23 ± 0.07	0.25 ± 0.09
liver	9.24 ± 1.12	18.41± 0.58	22.54 ± 1.93	19.07 ± 0.18	8.04 ± 0.84	20.04 ± 1.16	22.21 ± 2.74	22.38 ± 3.35
spleen	5.83 ± 0.36	12.61± 2.19	23.01 ± 2.87	26.85± 0.77	0.38 ± 0.01	1.03 ± 0.04	1.63 ± 0.31	1.71 ± 0.14
kidney	7.30 ± 0.93	4.99 ± 0.19	2.71 ± 0.29	3.00 ± 2.05	2.01 ± 0.21	1.75 ± 0.16	0.80 ± 0.16	0.98 ± 0.54
muscle	0.49 ± 0.08	0.63 ± 0.23	0.27 ± 0.07	0.37 ± 0.17	4.36 ± 0.76	5.97 ± 2.37	2.26 ± 0.55	3.18 ± 1.37
fat	0.46 ± 0.10	0.43 ± 0.11	0.27 ± 0.06	0.18 ± 0.03	1.42 ± 0.27	1.36 ± 0.27	0.76 ± 0.18	0.54 ± 0.07
heart	4.62 ± 0.53	4.41 ± 0.76	1.28 ± 0.28	0.98 ± 0.31	0.49 ± 0.06	0.54 ± 0.13	0.12 ± 0.03	0.11 ± 0.03
stomach	1.60 ± 0.34	1.25 ± 0.35	0.95 ± 0.14	0.78 ± 0.20	0.34 ± 0.04	0.34 ± 0.00	0.27 ± 0.03	0.17 ± 0.03
intestines	1.25 ± 0.08	0.97 ± 0.31	0.68 ± 0.06	0.87 ± 0.55	2.09 ± 0.02	1.99 ± 0.48	1.39 ± 0.20	1.50 ± 0.55
femur	4.81 ± 1.84	9.02 ± 1.48	20.03 ± 1.73	23.08 ± 0.85	13.28 ± 0.19	22.33 ±2.53	44.62 ± 3.95	54.02 ± 1.01

Table 12. The biodistribution of NUSPION-2 in normal Balb/c mice (n = 4). Data are presented as %ID/g ± s.d. and %ID/organ ± s.d.

organ	%ID/g				%ID/organ			
	1 h	4 h	24 h	48 h	1 h	4 h	24 h	48 h
blood	5.34 ± 0.38	1.11 ± 0.12	0.09 ± 0.01	0.05 ± 0.01	6.65 ± 0.47	1.60 ± 0.25	0.13 ± 0.01	0.08 ± 0.02
lung	7.40 ± 0.82	3.12 ± 0.43	1.22 ± 0.21	1.36 ± 0.20	0.94 ± 0.11	0.39 ± 0.05	0.17 ± 0.02	0.18 ± 0.04
liver	43.45 ±3.55	32.80 ± 3.88	40.57 ± 6.02	36.80 ± 1.88	41.74 ±1.70	36.27 ± 3.95	40.18 ± 2.33	40.68 ± 1.20
spleen	30.05±1.36	20.20 ± 4.85	25.78 ± 3.88	24.69 ± 4.04	2.05 ± 0.23	1.55 ± 0.72	1.90 ± 0.50	1.40 ± 0.64
kidney	3.47 ±0.34	3.20 ± 0.62	1.91 ± 0.17	1.23 ± 0.19	0.94 ± 0.03	0.95 ± 0.22	0.52 ± 0.10	0.36 ± 0.05
muscle	1.60 ±0.42	0.56 ± 0.08	0.61 ± 0.18	0.56 ± 0.11	11.72 ±3.18	4.70 ± 0.80	5.26 ± 1.72	4.93 ± 1.04
fat	0.58 ± 0.10	0.29 ± 0.19	0.33 ± 0.18	0.50 ± 0.46	1.43 ± 0.27	0.82 ± 0.52	0.96 ± 0.55	1.45 ± 1.31
heart	1.13 ± 0.60	0.53 ± 0.09	0.43 ± 0.09	0.71 ± 0.66	0.13 ± 0.03	0.09 ± 0.04	0.04 ± 0.01	0.07 ± 0.07
stomach	1.71 ± 0.54	0.82 ± 0.24	1.34 ± 0.48	0.70 ± 0.15	0.33 ± 0.11	0.26 ± 0.04	0.29 ± 0.07	0.26 ± 0.03
intestines	1.10 ± 0.17	0.90 ± 0.14	0.49 ± 0.04	0.34 ± 0.04	1.70 ± 0.23	1.52 ± 0.16	0.88 ± 0.09	0.70 ± 0.07

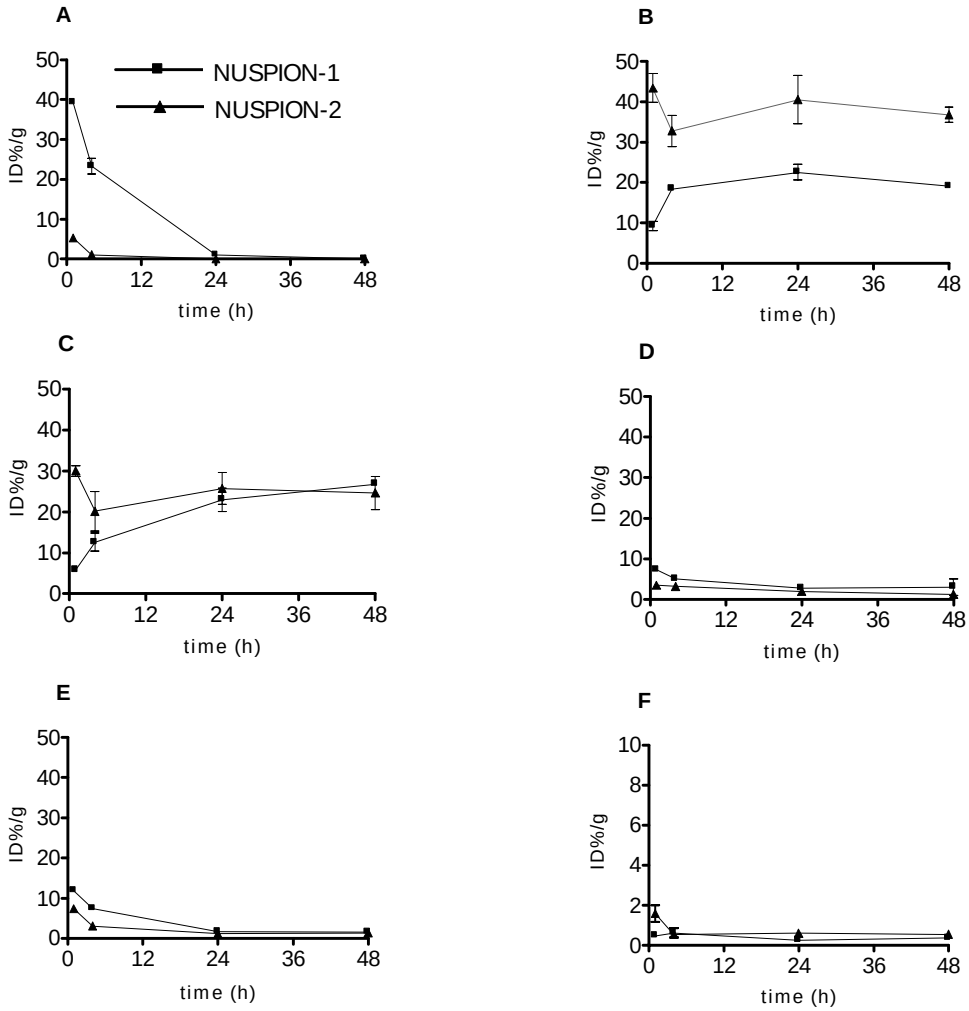

Figure 15. The time-activity curves of NUSPIONs in normal Balb/c mice in (A) blood, (B) liver, (C) spleen, (D) kidney, (E) lung, (F) muscle. Data are presented as %ID/g ± s.d.

Biodistribution in PC-3 tumor-bearing mice

In normal Balb/c mice, NUSPION-1 showed significant higher blood uptake and less accumulation in liver and spleen than NUSPION-2 at both 1 h ($p < 0.0001$) and 4 h p.i. ($p < 0.0001$), which are the desirable features for both passive and active targeting of tumors. It was thus used for further *in vivo* evaluation in a tumor-bearing animal model. Meanwhile, the NUSPION-1 was conjugated with R11 for prostate cancer targeting. The biodistribution results of NUSPION-1 and NUSPION-1-R11 in PC-3 tumor-bearing mice are presented in Tables 13, 14 and **Figure 16.** The tumor-to-muscle (T/M) and

tumor-to-blood (T/B) ratios are summarized in Table 15. Impressively the tumor had significant higher uptake than muscle ($p < 0.005$), blood ($p < 0.005$) and other organs ($p < 0.05$) except liver, spleen, lung (at 48 h p.i.) and kidney. NUSPION-1 showed as much as 2.2 %ID/g uptake at 24 h p.i. and 1.2 %ID/g at 48 h p.i. The mean ratios of T/M and T/B of NUSPION-1 are above 10 at both 24 h and 48 h p.i. The tumor targeting was likely resulted from the enhanced EPR effect due to the leaky vasculature and poor lymphatic drainage in solid tumors.

It is reasonable to assume that the targeting property of NUSPION-1 would be improved once tumor targeting molecules are used. However, NUSPION-1-R11 did not show increased tumor accumulation compared with non-targeted NUSPION-1, which is likely due to the significantly increased particle size that resulted in twice as much uptake in liver. However, NUSPION-1-R11 still showed high T/M (6.13 folds at 24 h p.i.) and T/B ratios (7.93 folds at 24 h. p.i.). The R11 conjugation should be optimized to minimize the aggregation.

The uptake data of NUSPION-1 in major organs are compared between normal and PC-3 tumor-bearing mice at 24-h p.i. and 48-h p.i. (**Figure 17**). Apparently the nanoparticle behaved similarly in the two mouse models. However, the absolute values of uptake in liver varied significantly ($p = 0.0004$) from 22.54 ± 1.93 %ID/g in normal mice to 14.89 ± 0.94 %ID/g in PC-3 tumor-bearing mice at 24 h p.i. while there was no significant difference ($p > 0.05$) at 48 h p.i. Likewise, spleen uptake varied significantly ($p = 0.0001$) from 26.85 ± 0.77 %ID/g in normal mice to 17.39 ± 2.02 %ID/g in PC-3 tumor-bearing mice at 48 h p.i. while there was no significant difference ($p > 0.05$) at 24 h p.i. The discrepancy of liver and spleen uptake in these two animal models was likely caused by the animal strain difference or by the biological changes resulted from the tumor burden.

Table 13. The biodistribution of NUSPION-1 in PC-3 tumor-bearing mice (n = 4). Data are presented as %ID/g ± s.d. and %ID/organ ± s.d.

organ	%ID/g		%ID/organ	
	24 h	48 h	24 h	48 h
blood	0.17 ± 0.01	0.03 ± 0.02	0.33 ± 0.03	0.07 ± 0.04
lung	0.99 ± 0.27	0.94 ± 0.41	0.16 ± 0.05	0.15 ± 0.05
liver	14.89 ± 0.94	17.69 ± 1.44	19.95 ± 0.91	20.70 ± 2.19
spleen	27.99 ± 3.56	17.39 ± 2.02	2.06 ± 0.79	1.85 ± 0.22
kidney	2.13 ± 0.15	1.83 ± 0.27	0.86 ± 0.16	0.72 ± 0.07
muscle	0.21 ± 0.29	0.07 ± 0.05	0.84 ± 1.45	0.77 ± 0.57
fat	0.11 ± 0.05	0.14 ± 0.13	0.42 ± 0.20	0.53 ± 0.47
heart	0.34 ± 0.11	0.38 ± 0.04	0.04 ± 0.01	0.04 ± 0.01
stomach	0.54 ± 0.26	0.52 ± 0.14	0.25 ± 0.11	0.19 ± 0.04
intestines	0.25 ± 0.07	0.34 ± 0.11	0.67 ± 0.13	0.91 ± 0.24
tumor	2.20 ± 0.83	1.18 ± 0.39		

Table 14. The biodistribution of NUSPION-1-R11 in PC-3 tumor-bearing mice (n = 4). Data are presented as %ID/g ± s.d. and %ID/organ ± s.d.

organ	%ID/g		%ID/organ	
	24 h	48 h	24 h	48 h
blood	0.10 ± 0.03	0.04 ± 0.01	0.19 ± 0.04	0.08 ± 0.03
lung	0.70 ± 0.15	0.48 ± 0.09	0.11 ± 0.02	0.08 ± 0.02
liver	45.50 ± 3.09	47.28 ± 7.59	58.27 ± 4.56	54.00 ± 2.42
spleen	20.25 ± 3.63	18.27 ± 5.29	1.94 ± 0.13	2.00 ± 0.40
kidney	0.91 ± 0.13	0.99 ± 0.24	0.38 ± 0.04	0.34 ± 0.04
muscle	0.14 ± 0.13	0.21 ± 0.05	1.56 ± 1.43	2.35 ± 0.54
fat	0.07 ± 0.12	0.14 ± 0.14	0.30 ± 0.47	0.53 ± 0.51
heart	0.25 ± 0.07	0.24 ± 0.04	0.03 ± 0.01	0.03 ± 0.01
stomach	0.17 ± 0.04	0.37 ± 0.21	0.10 ± 0.03	0.21 ± 0.13
intestines	0.08 ± 0.02	0.28 ± 0.12	0.22 ± 0.08	0.82 ± 0.30
tumor	1.01 ± 0.50	0.85 ± 0.35		

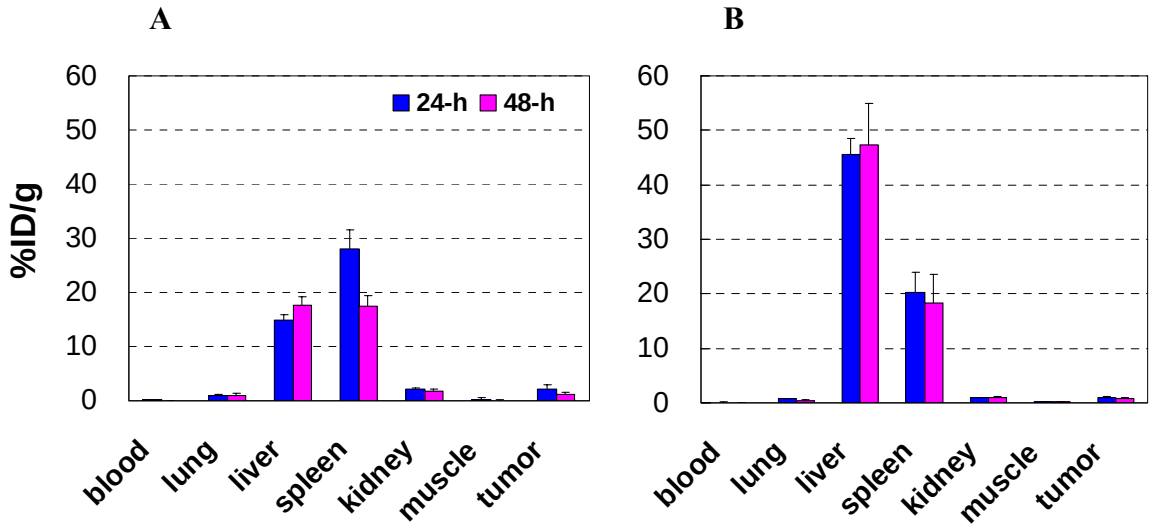

Figure 16. Biodistribution of NUSPIONs in PC-3 tumor-bearing mice with (A) NUSPION-1 and (B) NUSPION-1-R11. Data are presented as measured radioactivity in blood, lung, liver, spleen, kidney, muscle and tumor (%ID/organ ± s.d., n = 4).

Table 15. Tumor to blood and tumor to muscle ratios from biodistribution studies with NUSPION-1 and NUSPION-1-R11 in PC-3 tumor-bearing mice at 24 h and 48 h p.i. Data are present by the average uptake of the two tumors (left and right) divided by the uptake of blood or muscle

	24 h		48 h	
	NUSPION-1	NUSPION-1-R11	NUSPION-1	NUSPION-1-R11
T/M	11.12 ± 4.19	6.13 ± 0.74	12.20 ± 4.84	4.49 ± 2.49
T/B	12.07 ± 4.26	7.93 ± 0.16	28.90 ± 17.67	25.72 ± 17.30

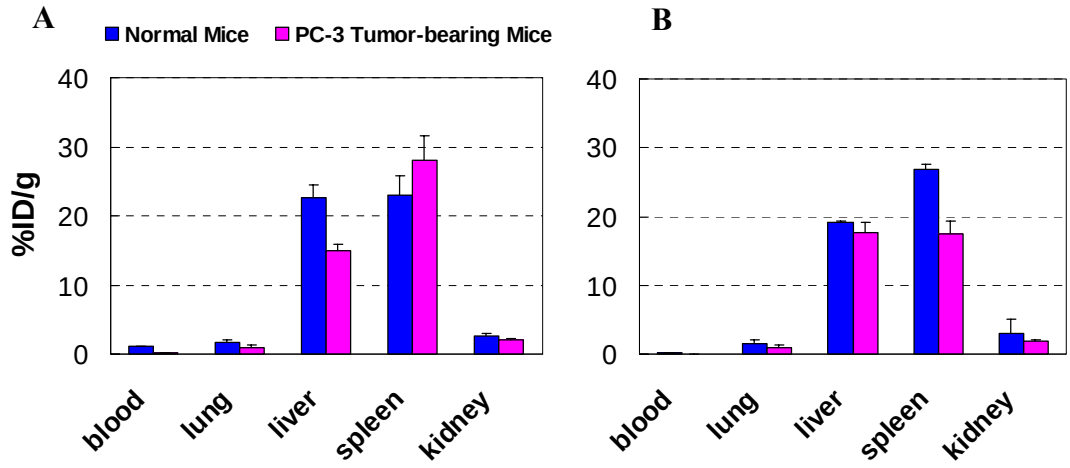

Figure 17. Comparative biodistribution data of NUSPION-1 in normal and PC-3 tumor-bearing mice at (A) 24 h p.i. and (B) 48 h p.i. Data are presented as %ID/g ± s.d.

MRI of PC-3 tumor-bearing mice

In order to evaluate the potential of the CLIONPs as MR imaging probes for *in vivo* application, five PC-3 tumor-bearing mice were used for MRI studies. Mouse #2 died before the 48 h measurement could be performed and hence only three time points were considered for this mouse. T_2-weighted images and T_2 maps of a slice through a PC-3 tumor (T) of mouse #3 were shown in **Figure 18**. Mean T_2 values from pooled voxels of all tumors (n = 5) at different time points were compared with the baseline collected before the injection by using GEE (Generalized Estimating Equations) method which accounts for intraclass correlations, with $p < 0.05$ considering to be significant different. At 3 h p.i., a small but statistically significant decrease ($p = 0.0041$) was observed (compared to pre-injection) in the mean T_2 value from 55.0 ± 0.2 ms to 53.5 ± 0.2 ms (mean ± SE) whereas no statistically significant difference was observed at 1 h p.i. If all the three time points are compared (pre vs 1 h p.i. vs 3 h p.i.), the decreasing trend is significant ($p = 0.0015$).

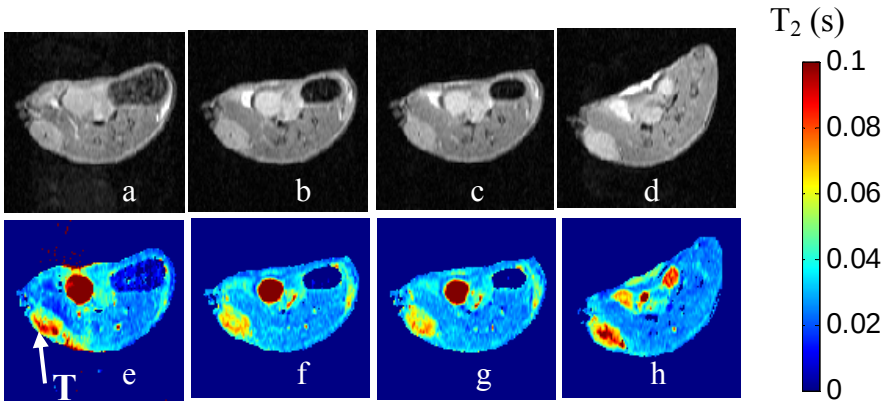

Figure 18. T_2-weighted images (*a*-d) and T_2 maps (e-f) of a slice through a PC-3 tumor (T) of mouse #3 (representative), pre (a, e), 1 h p.i. (b, f), 3 h p.i. (c, g) and 48 h p.i. (d, h) of CLIONP-1 (0.2 mmole Fe/ kg wt).

Prussian blue iron stain for tumoral iron measurement

Histochemistry analysis of the tumor slices after MRI study was carried out to verify the presence of iron oxide nanoparticles in the tumors. Shown in **Figure 19**, intracellular iron was visualized as blue granules in Prussian blue staining while the nuclei of cells was stained red and the cytoplasm pink. It is apparent that an appreciable amount of iron oxide nanoparticles was accumulated in the tumor.

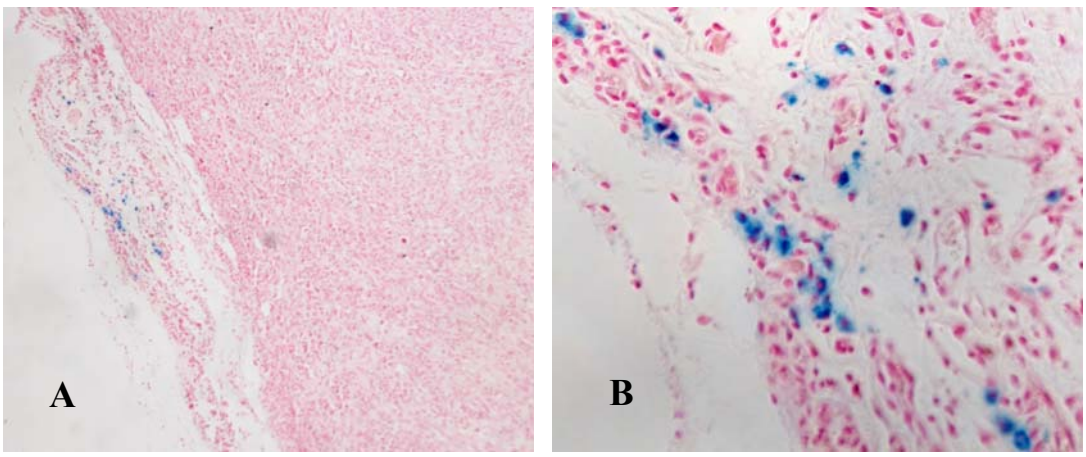

Figure 19. Prussian blue staining for tumoral iron determination. (A) Mouse # 3 right tumor at lower magnification (4X), (B) Mouse # 3 right tumor at higher magnification (20 X).

Autoradiography and post-autoradiography biodistribution studies

Autoradiography images of NUSPION-1 and NUSPION-2 in PC-3 tumor-bearing mice at 24 h p.i. are shown in **Figure 20**, from which the tumors were clearly visualized. The grayscale image files were analyzed using the associated Optiquant software after delineating the specific regions of interest (red circles) as shown in **Figure 20**. Data output in digital light units (DLU/mm^2) were imported into Microsoft Excel files for calculation of the T/M ratio based on the DLU. The ratio of DLU between tumor and muscle for NUSPION-1 is 1.73 while for NUSPION-2 is 1.34 at 24 h p.i.

The post-autoradiography biodistribution data after 72 h p.i. of NUSPION-1 and NUSPION-2 is summarized and compared (**Figure 21**). Surprisingly, at 72 h p.i., the spleen uptake of NUSPION-1 is significantly higher ($p = 0.0003$) than that of NUSPION-2 and there is no significant difference between liver uptake ($p > 0.05$).

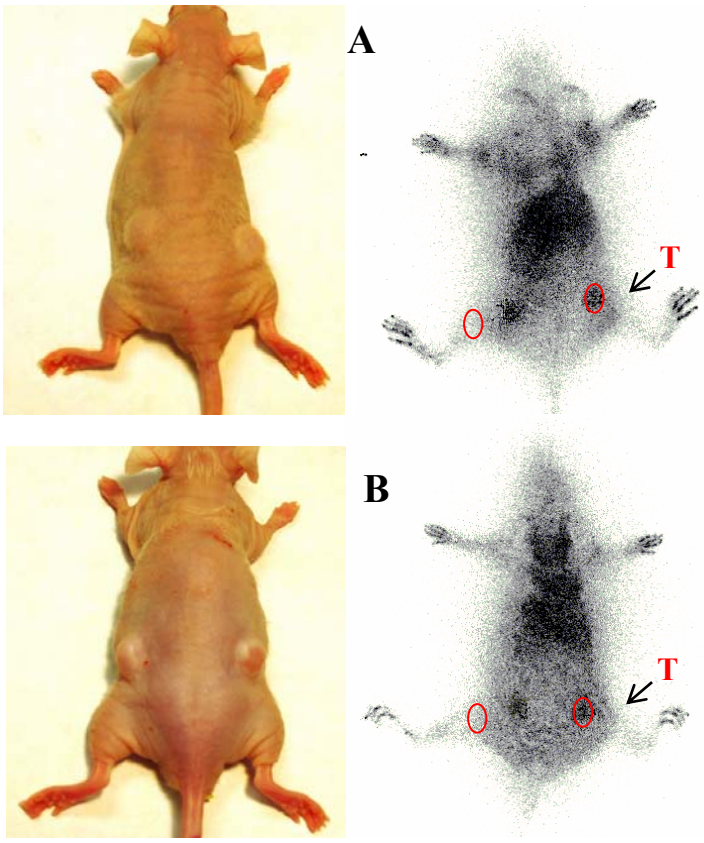

Figure 20. White light pictures (ventral view) and autoradiography images (dorsal view) of (A) NUSPION-1 and (B) NUSPION-2 in PC-3 tumor-bearing mice at 24 h p.i. The

arrows indicate the tumors and the circles are the quantization regions of tumor and muscle for the calculation of digital light unit ratio of tumor to muscle.

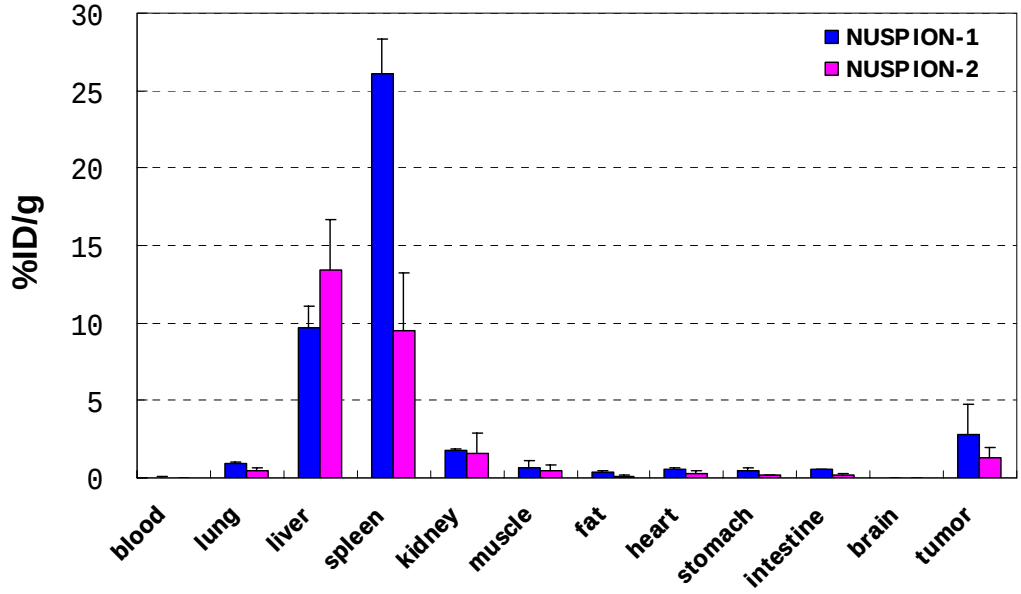

Figure 21. Comparative biodistribution data of NUSPION-1 and NUSPION-2 in PC-3 tumor-bearing mice at 72 h p.i. (post autoradiography) (n = 3). Data are presented as %ID/g ± s.d.

As demonstrated above, PC-3 tumors can be simultaneously visualized by both MRI and autoradiography. Both the post-autoradiography biodistribution and the post-MRI iron staining results confirmed that the nanoparticles indeed accumulated in the tumors. However we must point out that due to the radiation safety restrictions, the above *in vivo* imaging studies were not performed with a single injection dose, although a rigorous control was applied in the nanoparticle synthesis and injection dose preparation procedures to have the animals receive a virtual single dose. We anticipate that this drawback in our current design will be overcome in our future work once the radiation safety issues are addressed in the MRI studies.

CHAPTER 4 CONCLUSION AND PERSPECTIVES

Conclusion

A practical and reliable route has been developed to prepare dual-modality imaging probes by incorporating positron- or gamma emitters into the core of dextran-coated superparamagnetic iron oxide nanoparticles. To the best of our knowledge, no such synthetic strategies have been reported as a way to enable multi-modality imaging. By our method, the nanoparticles featuring a typical core/shell structure can be prepared with desired sizes with low polydispersity in a controllable manner. In this thesis, two distinctly sized nanoparticles were used for *in vivo* evaluation of the effects of particle size on the biodistribution in normal mice. As expected, the smaller particle presents higher uptake and longer retention time in blood, and less accumulation in RES organs such as liver and spleen compared to the larger one. Therefore, the smaller one was chosen for the further biodistribution and imaging studies in PC-3 tumor-bearing mice. Consistent with the high tumor uptake and high contrast of tumor to muscle and tumor to blood observed in the biodistribution studies, our proof-of concept MRI and autoradiography images clearly revealed the presence of the nanoparticles in the tumor, demonstrating the potential of the nanoparticles for *in vivo* dual-modality imaging. In addition, a method for surface modification and functionalization for active targeting has been successfully established. The satisfactory incorporation yield of radioisotopes, high stability, and good magnetic properties potentiate these nanoparticles for non-invasive dual-modality (MR/nuclear) imaging of cancer. Although this thesis has focused on prostate cancer targeting, it is apparent that the applications of the dual-modality imaging probes can be extended to other cancers as well by inclusion of the corresponding specific targeting molecules.

Perspectives

The goal of this project is to realize the early detection of primary and/or distal prostate cancer with high sensitivity and specificity by a non-invasive dual-modality imaging approach. For the active targeting of prostate cancer, we proposed to use four groups of typical targeting molecules. Limited by time, this thesis only used a peptide (R11) for the purpose. Given that the methodology has been developed, our future work will employ other targeting strategies. These include the use of a PSMA antibody E6 as a representative of antibodies, xPSM-A10-3 as a representative of aptamers, and GPI (2-[((3-amino-3-carboxypropyl) (hydroxy) phosphinyl)-methyl] pentane-1, 5-dioic acid as a representative of small organic molecules.

The application of these nanoparticles for therapy will be an extension of this project. With the proper choice of the loading amount of a therapeutic radioisotope into the core of nanoparticles or by attaching therapeutic agents onto the surface, it is straightforward to use these nanoscaffolds for the treatment of tumors and enable in situ dual-modality monitoring of the therapeutic efficacy.

BIBLIOGRAPHY

(1) Mankoff, D. A. (2007) A definition of molecular imaging. *J Nucl Med 48*, 18N, 21N.

(2) Brindle, K. (2008) New approaches for imaging tumour responses to treatment. *Nat Rev Cancer 8*, 94-107.

(3) Weissleder, R. (2002) Scaling down imaging: molecular mapping of cancer in mice. *Nat Rev Cancer 2*, 11-8.

(4) Rudin, M., and Weissleder, R. (2003) Molecular imaging in drug discovery and development. *Nat Rev Drug Discov 2*, 123-31.

(5) Massoud, T. F., and Gambhir, S. S. (2003) Molecular imaging in living subjects: seeing fundamental biological processes in a new light. *Genes Dev. 17*, 545-580.

(6) Garon, E. B., Marcu, L., Luong, Q., Tcherniantchouk, O., Crooks, G. M., and Koeffler, H. P. (2007) Quantum dot labeling and tracking of human leukemic, bone marrow and cord blood cells. *Leuk Res 31*, 643-51.

(7) Hargreaves, R. J. (2008) The role of molecular imaging in drug discovery and development. *Clin Pharmacol Ther 83*, 349-53.

(8) Dobrucki, L. W., and Sinusas, A. J. (2007) Imaging angiogenesis. *Curr Opin Biotechnol 18*, 90-6.

(9) Deckers, R., Rome, C., and Moonen, C. T. (2008) The role of ultrasound and magnetic resonance in local drug delivery. *J Magn Reson Imaging 27*, 400-9.

(10) McNally, E. G. (2008) Ultrasound of the small joints of the hands and feet: current status. *Skeletal Radiol 37*, 99-113.

(11) Mitragotri, S. (2005) Healing sound: the use of ultrasound in drug delivery and other therapeutic applications. *Nat Rev Drug Discov 4*, 255-60.

(12) Sosnovik, D. E., and Weissleder, R. (2007) Emerging concepts in molecular MRI. *Curr Opin Biotechnol 18*, 4-10.

(13) Lanza, G. M., Winter, P. M., Caruthers, S. D., Morawski, A. M., Schmieder, A. H., Crowder, K. C., and Wickline, S. A. (2004) Magnetic resonance molecular imaging with nanoparticles. *J Nucl Cardiol 11*, 733-43.

(14) Goldman, L. W. (2007) Principles of CT: radiation dose and image quality. *J Nucl Med Technol 35*, 213-25; quiz 226-8.

(15) Ohlerth, S., and Scharf, G. (2007) Computed tomography in small animals--basic principles and state of the art applications. *Vet J 173*, 254-71.

(16) Stanford, W. (2005) Advances in cardiovascular CT imaging: CT clinical imaging. *Int J Cardiovasc Imaging 21*, 29-37.

(17) Rembielak, A., Cullen, J., Saleem, A., and Price, P. (2008) Imaging in cancer. *Medicine 36*, 5-8.

(18) Hutchins, G. D., Miller, M. A., Soon, V. C., and Receveur, T. (2008) Small animal PET imaging. *Ilar J 49*, 54-65.

(19) Walker, R. C., Purnell, G. L., Jones-Jackson, L. B., Thomas, K. L., Brito, J. A., and Ferris, E. J. (2004) Introduction to PET Imaging with Emphasis on Biomedical Research. *NeuroToxicology 25*, 533-542.

(20) Sharma, S., and Ebadi, M. (2008) SPECT neuroimaging in translational research of CNS disorders. *Neurochem Int 52*, 352-62.

(21) Townsend, D. W. (2004) Physical principles and technology of clinical PET imaging. *Ann Acad Med Singapore 33*, 133-45.

(22) Budinger, T. F., Derenzo, S. E., Gullberg, G. T., Greenberg, W. L., and Huesman, R. H. (1977) Emission computer assisted tomography with single-photon and positron annihilation photon emitters. *J Comput Assist Tomogr 1*, 131-45.

(23) Cai, W., and Chen, X. (2007) Nanoplatforms for targeted molecular imaging in living subjects. *Small 3*, 1840-54.

(24) Welsh, D. K., and Kay, S. A. (2005) Bioluminescence imaging in living organisms. *Curr Opin Biotechnol 16*, 73-8.

(25) Negrin, R. S., and Contag, C. H. (2006) In vivo imaging using bioluminescence: a tool for probing graft-versus-host disease. *Nat Rev Immunol 6*, 484-490.

(26) Contag, C. H., and Bachmann, M. H. (2002) Advances in in vivo bioluminescence imaging of gene expression. *Annu Rev Biomed Eng 4*, 235-60.

(27) Wunder, A., and Klohs, J. (2008) Optical imaging of vascular pathophysiology. *Basic Res Cardiol 103*, 182-90.

(28) Sadikot, R. T., and Blackwell, T. S. (2005) Bioluminescence imaging. *Proc Am Thorac Soc 2*, 537-40, 511-2.

(29) Hilger, I., Leistner, Y., Berndt, A., Fritsche, C., Haas, K. M., Kosmehl, H., and Kaiser, W. A. (2004) Near-infrared fluorescence imaging of HER-2 protein over-expression in tumour cells. *Eur Radiol 14*, 1124-9.

(30) Ntziachristos, V., Bremer, C., and Weissleder, R. (2003) Fluorescence imaging with near-infrared light: new technological advances that enable in vivo molecular imaging. *Eur Radiol 13*, 195-208.

(31) Ntziachristos, V. (2006) Fluorescence molecular imaging. *Annu Rev Biomed Eng 8*, 1-33.

(32) Luker, G. D., and Luker, K. E. (2008) Optical imaging: current applications and future directions. *J Nucl Med 49*, 1-4.

(33) Culver, J., Akers, W., and Achilefu, S. (2008) Multimodality Molecular Imaging with Combined Optical and SPECT/PET Modalities. *J Nucl Med 49*, 169-72.

(34) van Vlerken, L. E., and Amiji, M. M. (2006) Multi-functional polymeric nanoparticles for tumour-targeted drug delivery. *Expert Opin Drug Deliv 3*, 205-16.

(35) Kim, J. H., Lee, S., Park, K., Nam, H. Y., Jang, S. Y., Youn, I., Kim, K., Jeon, H., Park, R. W., Kim, I. S., Choi, K., and Kwon, I. C. (2007) Protein-phosphorylation-responsive polymeric nanoparticles for imaging protein kinase activities in single living cells. *Angew Chem Int Ed Engl 46*, 5779-82.

(36) Owens, D. E., 3rd, and Peppas, N. A. (2006) Opsonization, biodistribution, and pharmacokinetics of polymeric nanoparticles. *Int J Pharm 307*, 93-102.

(37) Win, K. Y., and Feng, S. S. (2005) Effects of particle size and surface coating on cellular uptake of polymeric nanoparticles for oral delivery of anticancer drugs. *Biomaterials 26*, 2713-22.

(38) Soppimath, K. S., Aminabhavi, T. M., Kulkarni, A. R., and Rudzinski, W. E. (2001) Biodegradable polymeric nanoparticles as drug delivery devices. *J Control Release 70*, 1-20.

(39) Wang, X., Yang, L., Chen, Z. G., and Shin, D. M. (2008) Application of Nanotechnology in Cancer Therapy and Imaging. *CA Cancer J Clin*.

(40) Li, X., Shi, J., Zhu, Y., Shen, W., Li, H., Liang, J., and Gao, J. (2007) A template route to the preparation of mesoporous amorphous calcium silicate with high in vitro bone-forming bioactivity. *J Biomed Mater Res B Appl Biomater 83*, 431-9.

(41) Thorek, D. L., Chen, A. K., Czupryna, J., and Tsourkas, A. (2006) Superparamagnetic iron oxide nanoparticle probes for molecular imaging. *Ann Biomed Eng 34*, 23-38.

(42) Rogers, W. J., and Basu, P. (2005) Factors regulating macrophage endocytosis of nanoparticles: implications for targeted magnetic resonance plaque imaging. *Atherosclerosis 178*, 67-73.

(43) Raynal, I., Prigent, P., Peyramaure, S., Najid, A., Rebuzzi, C., and Corot, C. (2004) Macrophage endocytosis of superparamagnetic iron oxide nanoparticles: mechanisms and comparison of ferumoxides and ferumoxtran-10. *Invest Radiol 39*, 56-63.

(44) Lee, H., Yu, M. K., Park, S., Moon, S., Min, J. J., Jeong, Y. Y., Kang, H. W., and Jon, S. (2007) Thermally cross-linked superparamagnetic iron oxide nanoparticles: synthesis and application as a dual imaging probe for cancer in vivo. *J Am Chem Soc 129*, 12739-45.

(45) Liu, P. K., Mandeville, J. B., Dai, G., Jenkins, B. G., Kim, Y. R., and Liu, C. H. (2007) Transcription MRI: A New View of the Living Brain. *Neuroscientist*.

(46) Ma, H. L., Qi, X. R., Maitani, Y., and Nagai, T. (2007) Preparation and characterization of superparamagnetic iron oxide nanoparticles stabilized by alginate. *Int J Pharm 333*, 177-86.

(47) von Zur Muhlen, C., von Elverfeldt, D., Bassler, N., Neudorfer, I., Steitz, B., Petri-Fink, A., Hofmann, H., Bode, C., and Peter, K. (2007) Superparamagnetic iron oxide binding and uptake as imaged by magnetic resonance is mediated by the integrin receptor Mac-1 (CD11b/CD18): implications on imaging of atherosclerotic plaques. *Atherosclerosis 193*,

102-11.

(48) Nasongkla, N., Bey, E., Ren, J., Ai, H., Khemtong, C., Guthi, J. S., Chin, S. F., Sherry, A. D., Boothman, D. A., and Gao, J. (2006) Multifunctional polymeric micelles as cancer-targeted, MRI-ultrasensitive drug delivery systems. *Nano Lett 6*, 2427-30.

(49) Sosnovik, D. E., Nahrendorf, M., and Weissleder, R. (2007) Molecular magnetic resonance imaging in cardiovascular medicine. *Circulation 115*, 2076-86.

(50) Wu, Y. J., Muldoon, L. L., Varallyay, C., Markwardt, S., Jones, R. E., and Neuwelt, E. A. (2007) In vivo leukocyte labeling with intravenous ferumoxides/protamine sulfate complex and in vitro characterization for cellular magnetic resonance imaging. *Am J Physiol Cell Physiol 293*, C1698-708.

(51) Moghimi, S. M., Hunter, A. C., and Murray, J. C. (2001) Long-circulating and target-specific nanoparticles: theory to practice. *Pharmacol Rev 53*, 283-318.

(52) Yezhelyev, M. V., Gao, X., Xing, Y., Al-Hajj, A., Nie, S., and O'Regan, R. M. (2006) Emerging use of nanoparticles in diagnosis and treatment of breast cancer. *Lancet Oncol 7*, 657-67.

(53) Manchester, M., and Singh, P. (2006) Virus-based nanoparticles (VNPs): Platform technologies for diagnostic imaging. *Adv Drug Deliv Rev 58*, 1505-22.

(54) Wang, S., and Low, P. S. (1998) Folate-mediated targeting of antineoplastic drugs, imaging agents, and nucleic acids to cancer cells. *J Control Release 53*, 39-48.

(55) Mulder, W. J., Strijkers, G. J., van Tilborg, G. A., Griffioen, A. W., and Nicolay, K. (2006) Lipid-based nanoparticles for contrast-enhanced MRI and molecular imaging. *NMR Biomed 19*, 142-64.

(56) Sawant, R. M., Hurley, J. P., Salmaso, S., Kale, A., Tolcheva, E., Levchenko, T. S., and Torchilin, V. P. (2006) "SMART" drug delivery systems: double-targeted pH-responsive pharmaceutical nanocarriers. *Bioconjug Chem 17*, 943-9.

(57) Torchilin, V. P. (2007) Targeted pharmaceutical nanocarriers for cancer therapy and imaging. *Aaps J 9*, E128-47.

(58) Portney, N. G., and Ozkan, M. (2006) Nano-oncology: drug delivery, imaging, and sensing. *Anal Bioanal Chem 384*, 620-30.

(59) Groneberg, D. A., Giersig, M., Welte, T., and Pison, U. (2006) Nanoparticle-based diagnosis and therapy. *Curr Drug Targets 7*, 643-8.

(60) Pison, U., Welte, T., Giersig, M., and Groneberg, D. A. (2006) Nanomedicine for respiratory diseases. *Eur J Pharmacol 533*, 341-50.

(61) Michalet, X., Pinaud, F. F., Bentolila, L. A., Tsay, J. M., Doose, S., Li, J. J., Sundaresan, G., Wu, A. M., Gambhir, S. S., and Weiss, S. (2005) Quantum dots for live cells, in vivo imaging, and diagnostics. *Science 307*, 538-44.

(62) Liu, S., Lee, C. M., Wang, S., and Lu, D. R. (2006) A new bioimaging carrier for

fluorescent quantum dots: phospholipid nanoemulsion mimicking natural lipoprotein core. *Drug Deliv 13*, 159-64.

(63) Gao, X., Yang, L., Petros, J. A., Marshall, F. F., Simons, J. W., and Nie, S. (2005) In vivo molecular and cellular imaging with quantum dots. *Curr Opin Biotechnol 16*, 63-72.

(64) Medintz, I. L., Uyeda, H. T., Goldman, E. R., and Mattoussi, H. (2005) Quantum dot bioconjugates for imaging, labelling and sensing. *Nat Mater 4*, 435-46.

(65) Nie, S., Xing, Y., Kim, G. J., and Simons, J. W. (2007) Nanotechnology applications in cancer. *Annu Rev Biomed Eng 9*, 257-88.

(66) Le Gac, S., Vermes, I., and van den Berg, A. (2006) Quantum dots based probes conjugated to annexin V for photostable apoptosis detection and imaging. *Nano Lett 6*, 1863-9.

(67) Yong, K. T., Qian, J., Roy, I., Lee, H. H., Bergey, E. J., Tramposch, K. M., He, S., Swihart, M. T., Maitra, A., and Prasad, P. N. (2007) Quantum rod bioconjugates as targeted probes for confocal and two-photon fluorescence imaging of cancer cells. *Nano Lett 7*, 761-5.

(68) Wang, M. D., Shin, D. M., Simons, J. W., and Nie, S. (2007) Nanotechnology for targeted cancer therapy. *Expert Rev Anticancer Ther 7*, 833-7.

(69) Talanov, V. S., Regino, C. A., Kobayashi, H., Bernardo, M., Choyke, P. L., and Brechbiel, M. W. (2006) Dendrimer-based nanoprobe for dual modality magnetic resonance and fluorescence imaging. *Nano Lett 6*, 1459-63.

(70) Helms, B., and Meijer, E. W. (2006) Chemistry. Dendrimers at work. *Science 313*, 929-30.

(71) Caruthers, S. D., Winter, P. M., Wickline, S. A., and Lanza, G. M. (2006) Targeted magnetic resonance imaging contrast agents. *Methods Mol Med 124*, 387-400.

(72) Tomalia, D. A., Reyna, L. A., and Svenson, S. (2007) Dendrimers as multi-purpose nanodevices for oncology drug delivery and diagnostic imaging. *Biochem Soc Trans 35*, 61-7.

(73) Pan, B., Cui, D., Sheng, Y., Ozkan, C., Gao, F., He, R., Li, Q., Xu, P., and Huang, T. (2007) Dendrimer-modified magnetic nanoparticles enhance efficiency of gene delivery system. *Cancer Res 67*, 8156-63.

(74) Mitra, A., Nan, A., Line, B. R., and Ghandehari, H. (2006) Nanocarriers for nuclear imaging and radiotherapy of cancer. *Curr Pharm Des 12*, 4729-49.

(75) Weibo Cai, X. C. (2007) Nanoplatforms for Targeted Molecular Imaging in Living Subjects. *Small 3*, 1840-1854.

(76) Corot, C., Robert, P., Idee, J. M., and Port, M. (2006) Recent advances in iron oxide nanocrystal technology for medical imaging. *Adv Drug Deliv Rev 58*, 1471-504.

(77) Harisinghani, M. G., Barentsz, J., Hahn, P. F., Deserno, W. M., Tabatabaei, S., van de Kaa, C. H., de la Rosette, J., and Weissleder, R. (2003) Noninvasive Detection of Clinically

Occult Lymph-Node Metastases in Prostate Cancer. *N Engl J Med 348*, 2491-2499.

(78) Koh, D. M., Cook, G. J., and Husband, J. E. (2003) New horizons in oncologic imaging. *N Engl J Med 348*, 2487-8.

(79) Michel M.J.Modo, J. W. M. B. (2007) Molecular and Cellular MR Imaging.

(80) Sosnovik, D. E., Nahrendorf, M., and Weissleder, R. (2008) Magnetic nanoparticles for MR imaging: agents, techniques and cardiovascular applications. *Basic Res Cardiol 103*, 122-30.

(81) Frullano, L., and Meade, T. J. (2007) Multimodal MRI contrast agents. *J Biol Inorg Chem 12*, 939-49.

(82) DeNardo, S. J., DeNardo, G. L., Natarajan, A., Miers, L. A., Foreman, A. R., Gruettner, C., Adamson, G. N., and Ivkov, R. (2007) Thermal dosimetry predictive of efficacy of 111In-ChL6 nanoparticle AMF--induced thermoablative therapy for human breast cancer in mice. *J Nucl Med 48*, 437-44.

(83) Fang, J., Kumbhar, A., Zhou, W. L., and Stokes, K. L. (2003) Nanoneedles of maghemite iron oxide prepared from a wet chemical route. *Materials Research Bulletin 38*, 461-467.

(84) Bee, A., Massart, R., and Neveu, S. (1995) Synthesis of very fine maghemite particles. *Journal of Magnetism and Magnetic Materials 149*, 6-9.

(85) Ennas, G., Marongiu, G., Musinu, A., Falqui, A., Ballirano, P., and Caminiti, R. (1999) Characterization of nanocrystalline gama-Fe_2O_3 prepared by wet chemical method. *J. Mater. Res. 14*, 1570-5.

(86) Kang, Y. S., Risbud, S., Rabolt, J. F., and Stroeve, P. (1996) Synthesis and characterization of nanometer-size Fe_3O_4 and gamma-Fe_2O_3 particles. *Chem. Mater. 8*, 2209-11.

(87) Pascal, C., Pascal, J. L., Favier, F., Elidrissi, Moubtassim, M. L., and Payen, C. (1999) Electrochemical synthesis for the control of gamma-Fe_2O_3 nanoparticle size. morphology, microstructure, and magnetic behavior. *Chem. Mater. 11*, 141 - 147.

(88) Shafi, K. V. P. M., Ulman, A., Dyal, A., Yan, X. Z., Yang, N. L., Estournes, C., Fournes, L., Wattiaux, A., White, H., and Rafailovich, M. (2002) Magnetic enhancement of gamma-Fe_2O_3 nanoparticles by sonochemical coating. *Chem. Mater. 14*, 1778-1787.

(89) Martinez, B., Roig, A., Molins, E., Gonzalez-Carreno, T., and Serna, C. J. (1998) Magnetic characterization of gamma-Fe_2O_3 nanoparticles fabricated by aerosol pyrolysis. *J. Appl. Phys. 83*, 3256-62.

(90) Morales, M. P., Veintemillas-Verdaguer, S., and Serna, C. J. (1999) Magnetic properties of uniform g-Fe_2O_3 nanoparticles smaller than 5 nm prepared by laser pyrolysis. *J. Mater. Res. 14*, 3066-72.

(91) Hogemann, D., Ntziachristos, V., Josephson, L., and Weissleder, R. (2002) High throughput magnetic resonance imaging for evaluating targeted nanoparticle probes. *Bioconjugate Chem 13*, 116-21.

(92) Josephson, L., Kircher, M. F., Mahmood, U., Tang, Y., and Weissleder, R. (2002) Near-infrared fluorescent nanoparticles as combined MR/optical imaging probes. *Bioconjugate Chem 13*, 554-60.

(93) Josephson, L., Perez, J. M., and Weissleder, R. (2001) Magnetic nanosensors for the detection of oligonucleotide sequences. *Angew. Chem. Int. Ed. 40*, 3204-6.

(94) Josephson, L., Tung, C. H., Moore, A., and Weissleder, R. (1999) High-efficiency intracellular magnetic labeling with novel superparamagnetic-Tat peptide conjugates. *Bioconjugate Chem 10*, 186-91.

(95) Schellenberger, E. A., Hogemann, D., Josephson, L., and Weissleder, R. (2002) Annexin V-CLIO: a nanoparticle for detecting apoptosis by MRI. *Acad Radiol 9 Suppl 2*, S310-1.

(96) Wunderbaldinger, P., Josephson, L., and Weissleder, R. (2002) Tat peptide directs enhanced clearance and hepatic permeability of magnetic nanoparticles. *Bioconjugate Chem 13*, 264-8.

(97) Wunderbaldinger, P., Josephson, L., and Weissleder, R. (2002) Crosslinked iron oxides (CLIO): a new platform for the development of targeted MR contrast agents. *Acad Radiol 9 Suppl 2*, S304-6.

(98) Zhao, M., Kircher, M. F., Josephson, L., and Weissleder, R. (2002) Differential conjugation of tat peptide to superparamagnetic nanoparticles and its effect on cellular uptake. *Bioconjugate Chem 13*, 840-4.

(99) Weissleder, R., and Ntziachristos, V. (2003) Shedding light onto live molecular targets. *Nat Med 9*, 123-8.

(100) Josephson, L., Kircher, M. F., Mahmood, U., Tang, Y., and Weissleder, R. (2002) Near-infrared fluorescent nanoparticles as combined MR/optical imaging probes. *Bioconjug Chem 13*, 554-60.

(101) Sharma, P., Brown, S., Walter, G., Santra, S., and Moudgil, B. (2006) Nanoparticles for bioimaging. *Adv Colloid Interface Sci 123-126*, 471-85.

(102) Neri, D., and Bicknell, R. (2005) TUMOUR VASCULAR TARGETING. *Nature Reviews Cancer 5*, 436-446.

(103) Josephson, L., Tung, C. H., Moore, A., and Weissleder, R. (1999) High-efficiency intracellular magnetic labeling with novel superparamagnetic-Tat peptide conjugates. *Bioconjug Chem 10*, 186-91.

(104) Veronese, F. M. (2001) Peptide and protein PEGylation: a review of problems and solutions. *Biomaterials 22*, 405-417.

(105) Palmacci, S., and Josephson, L. (1993) Synthesis of polysaccharide covered superparamagnetic oxide colloids. *U.S. Patent 5,262,176.*

(106) Nassar, N. N., and Husein, M. M. (2007) Effect of microemulsion variables on copper oxide nanoparticle uptake by AOT microemulsions. *J Colloid Interface Sci 316*, 442-50.

(107) Yuan, H., Huang, L. F., Du, Y. Z., Ying, X. Y., You, J., Hu, F. Q., and Zeng, S. (2008) Solid lipid nanoparticles prepared by solvent diffusion method in a nanoreactor system. *Colloids Surf B Biointerfaces 61*, 132-7.

(108) Sun, E. Y., Josephson, L., Kelly, K. A., and Weissleder, R. (2006) Development of nanoparticle libraries for biosensing. *Bioconjug Chem 17*, 109-13.

(109) Schipper, M. L., Cheng, Z., Lee, S.-W., Bentolila, L. A., Iyer, G., Rao, J., Chen, X., Wu, A. M., Weiss, S., and Gambhir, S. S. (2007) microPET-Based Biodistribution of Quantum Dots in Living Mice. *J Nucl Med 48*, 1511-1518.

(110) Thanou, M., and Duncan, R. (2003) Polymer-protein and polymer-drug conjugates in cancer therapy. *Curr Opin Investig Drugs 4*, 701-9.

(111) Duncan, R. (2003) The dawning era of polymer therapeutics. *Nat Rev Drug Discov 2*, 347-60.

(112) Matsumura, Y., and Maeda, H. (1986) A new concept for macromolecular therapeutics in cancer chemotherapy: mechanism of tumoritropic accumulation of proteins and the antitumor agent smancs. *Cancer Res 46*, 6387-92.

(113) Bergen, J. M., von Recum, H. A., Goodman, T. T., Massey, A. P., and Pun, S. H. (2006) Gold nanoparticles as a versatile platform for optimizing physicochemical parameters for targeted drug delivery. *Macromol Biosci 6*, 506-16.

(114) Zhang, L., Sun, M., Guo, R., Jiang, Z., Liu, Y., Jiang, X., and Yang, C. (2006) Chitosan surface-modified hydroxycamptothecin loaded nanoparticles with enhanced transport across Caco-2 cell monolayer. *J Nanosci Nanotechnol 6*, 2912-20.

(115) Torchilin, V. P. (2005) Recent advances with liposomes as pharmaceutical carriers. *Nat Rev Drug Discov 4*, 145-60.

(116) Alexis, F., Rhee, J. W., Richie, J. P., Radovic-Moreno, A. F., Langer, R., and Farokhzad, O. C. (2008) New frontiers in nanotechnology for cancer treatment. *Urol Oncol 26*, 74-85.

(117) Montet, X., Funovics, M., Montet-Abou, K., Weissleder, R., and Josephson, L. (2006) Multivalent effects of RGD peptides obtained by nanoparticle display. *J Med Chem 49*, 6087-93.

(118) Dubey, P. K., Mishra, V., Jain, S., Mahor, S., and Vyas, S. P. (2004) Liposomes modified with cyclic RGD peptide for tumor targeting. *J Drug Target 12*, 257-64.

(119) Guccione, S., Li, K. C., and Bednarski, M. D. (2004) Vascular-targeted nanoparticles for molecular imaging and therapy. *Methods Enzymol 386*, 219-36.

(120) Hood, J. D., Bednarski, M., Frausto, R., Guccione, S., Reisfeld, R. A., Xiang, R., and Cheresh, D. A. (2002) Tumor regression by targeted gene delivery to the neovasculature. *Science 296*, 2404-7.

(121) Li, L., Wartchow, C. A., Danthi, S. N., Shen, Z., Dechene, N., Pease, J., Choi, H. S., Doede, T., Chu, P., Ning, S., Lee, D. Y., Bednarski, M. D., and Knox, S. J. (2004) A novel

antiangiogenesis therapy using an integrin antagonist or anti-Flk-1 antibody coated 90Y-labeled nanoparticles. *Int J Radiat Oncol Biol Phys 58*, 1215-27.

(122) Winter, P. M., Caruthers, S. D., Kassner, A., Harris, T. D., Chinen, L. K., Allen, J. S., Lacy, E. K., Zhang, H., Robertson, J. D., Wickline, S. A., and Lanza, G. M. (2003) Molecular imaging of angiogenesis in nascent Vx-2 rabbit tumors using a novel alpha(nu)beta3-targeted nanoparticle and 1.5 tesla magnetic resonance imaging. *Cancer Res 63*, 5838-43.

(123) Ghosh, A., and Heston, W. D. (2004) Tumor target prostate specific membrane antigen (PSMA) and its regulation in prostate cancer. *J Cell Biochem 91*, 528-39.

(124) Schulke, N., Varlamova, O. A., Donovan, G. P., Ma, D., Gardner, J. P., Morrissey, D. M., Arrigale, R. R., Zhan, C., Chodera, A. J., Surowitz, K. G., Maddon, P. J., Heston, W. D., and Olson, W. C. (2003) The homodimer of prostate-specific membrane antigen is a functional target for cancer therapy. *Proc Natl Acad Sci U S A 100*, 12590-5.

(125) Tasch, J., Gong, M., Sadelain, M., and Heston, W. D. (2001) A unique folate hydrolase, prostate-specific membrane antigen (PSMA): a target for immunotherapy? *Crit Rev Immunol 21*, 249-61.

(126) Gong, M. C., Chang, S. S., Watt, F., O'Keefe, D. S., Bacich, D. J., Uchida, A., Bander, N. H., Reuter, V. E., Gaudin, P. B., Molloy, P. L., Sadelian, M., and Heston, W. D. (2000) Overview of evolving strategies incorporating prostate-specific membrane antigen as target for therapy. *Mol Urol 4*, 217-22;discussion 223.

(127) Gong, M. C., Chang, S. S., Sadelain, M., Bander, N. H., and Heston, W. D. (1999) Prostate-specific membrane antigen (PSMA)-specific monoclonal antibodies in the treatment of prostate and other cancers. *Cancer Metastasis Rev 18*, 483-90.

(128) Lamb, H. M., and Faulds, D. (1998) Capromab pendetide. A review of its use as an imaging agent in prostate cancer. *Drugs Aging 12*, 293-304.

(129) Huang, X., Bennett, M., and Thorpe, P. E. (2004) Anti-tumor effects and lack of side effects in mice of an immunotoxin directed against human and mouse prostate-specific membrane antigen. *Prostate 61*, 1-11.

(130) Chang, S. S. (2004) Monoclonal antibodies and prostate-specific membrane antigen. *Curr Opin Investig Drugs 5*, 611-5.

(131) Chang, S. S., Reuter, V. E., Heston, W. D., Bander, N. H., Grauer, L. S., and Gaudin, P. B. (1999) Five different anti-prostate-specific membrane antigen (PSMA) antibodies confirm PSMA expression in tumor-associated neovasculature. *Cancer Res 59*, 3192-8.

(132) Liu, H., Moy, P., Kim, S., Xia, Y., Rajasekaran, A., Navarro, V., Knudsen, B., and Bander, N. H. (1997) Monoclonal antibodies to the extracellular domain of prostate-specific membrane antigen also react with tumor vascular endothelium. *Cancer Res 57*, 3629-34.

(133) Murphy, G. P., Greene, T. G., Tino, W. T., Boynton, A. L., and Holmes, E. H. (1998) Isolation and characterization of monoclonal antibodies specific for the extracellular domain of prostate specific membrane antigen. *J Urol 160*, 2396-401.

(134) Smith-Jones, P. M., Vallabhajosula, S., Navarro, V., Bastidas, D., Goldsmith, S. J., and Bander, N. H. (2003) Radiolabeled monoclonal antibodies specific to the extracellular domain of prostate-specific membrane antigen: preclinical studies in nude mice bearing LNCaP human prostate tumor. *J Nucl Med 44*, 610-7.

(135) Brody, E. N., and Gold, L. (2000) Aptamers as therapeutic and diagnostic agents. *J Biotechnol 74*, 5-13.

(136) Brody, E. N., Willis, M. C., Smith, J. D., Jayasena, S., Zichi, D., and Gold, L. (1999) The use of aptamers in large arrays for molecular diagnostics. *Mol Diagn 4*, 381-8.

(137) Ellington, A. D., and Szostak, J. W. (1990) In vitro selection of RNA molecules that bind specific ligands. *Nature 346*, 818-22.

(138) Ellington, A. D., and Szostak, J. W. (1992) Selection in vitro of single-stranded DNA molecules that fold into specific ligand-binding structures. *Nature 355*, 850-2.

(139) Gander, T. R., Brody, E. N., Mehler, R. E., Heilig, J. S., Singer, B. S., and Gold, L. (2003) Driving forces in cancer diagnostics. *MLO Med Lab Obs 35*, 10-6, 20; quiz 20-1.

(140) Gold, L., Singer, B., He, Y. Y., and Brody, E. (1997) SELEX and the evolution of genomes. *Curr Opin Genet Dev 7*, 848-51.

(141) Irvine, D., Tuerk, C., and Gold, L. (1991) SELEXION. Systematic evolution of ligands by exponential enrichment with integrated optimization by non-linear analysis. *J Mol Biol 222*, 739-61.

(142) Tuerk, C., and Gold, L. (1990) Systematic evolution of ligands by exponential enrichment: RNA ligands to bacteriophage T4 DNA polymerase. *Science 249*, 505-10.

(143) Hicke, B. J., and Stephens, A. W. (2000) Escort aptamers: a delivery service for diagnosis and therapy. *J Clin Invest 106*, 923-8.

(144) Jayasena, S. D. (1999) Aptamers: an emerging class of molecules that rival antibodies in diagnostics. *Clin Chem 45*, 1628-50.

(145) Lupold, S. E., Hicke, B. J., Lin, Y., and Coffey, D. S. (2002) Identification and characterization of nuclease-stabilized RNA molecules that bind human prostate cancer cells via the prostate-specific membrane antigen. *Cancer Res 62*, 4029-33.

(146) Farokhzad, O. C., Jon, S., Khademhosseini, A., Tran, T. N., Lavan, D. A., and Langer, R. (2004) Nanoparticle-aptamer bioconjugates: a new approach for targeting prostate cancer cells. *Cancer Res 64*, 7668-72.

(147) Serda, R. E., Adolphi, N. L., Bisoffi, M., and Sillerud, L. O. (2007) Targeting and cellular trafficking of magnetic nanoparticles for prostate cancer imaging. *Mol Imaging 6*, 277-88.

(148) Antony, A. C. (1996) Folate receptors. *Annu Rev Nutr 16*, 501-21.

(149) Garin-Chesa, P., Campbell, I., Saigo, P. E., Lewis, J. L., Jr., Old, L. J., and Rettig, W. J. (1993) Trophoblast and ovarian cancer antigen LK26. Sensitivity and specificity in immunopathology and molecular identification as a folate-binding protein. *Am J Pathol*

142, 557-67.

(150) Gabizon, A., Shmeeda, H., Horowitz, A. T., and Zalipsky, S. (2004) Tumor cell targeting of liposome-entrapped drugs with phospholipid-anchored folic acid-PEG conjugates. *Adv Drug Deliv Rev 56*, 1177-92.

(151) Leamon, C. P., Cooper, S. R., and Hardee, G. E. (2003) Folate-liposome-mediated antisense oligodeoxynucleotide targeting to cancer cells: evaluation in vitro and in vivo. *Bioconjug Chem 14*, 738-47.

(152) Leamon, C. P., and Reddy, J. A. (2004) Folate-targeted chemotherapy. *Adv Drug Deliv Rev 56*, 1127-41.

(153) Ke, C. Y., Mathias, C. J., and Green, M. A. (2003) The folate receptor as a molecular target for tumor-selective radionuclide delivery. *Nucl Med Biol 30*, 811-7.

(154) Turek, J. J., Leamon, C. P., and Low, P. S. (1993) Endocytosis of folate-protein conjugates: ultrastructural localization in KB cells. *J Cell Sci 106 (Pt 1)*, 423-30.

(155) Choi, H., Choi, S. R., Zhou, R., Kung, H. F., and Chen, I. W. (2004) Iron oxide nanoparticles as magnetic resonance contrast agent for tumor imaging via folate receptor-targeted delivery. *Acad Radiol 11*, 996-1004.

(156) Brooks, P. C., Clark, R. A., and Cheresh, D. A. (1994) Requirement of vascular integrin alpha v beta 3 for angiogenesis. *Science 264*, 569-71.

(157) Brooks, P. C., Montgomery, A. M., Rosenfeld, M., Reisfeld, R. A., Hu, T., Klier, G., and Cheresh, D. A. (1994) Integrin alpha v beta 3 antagonists promote tumor regression by inducing apoptosis of angiogenic blood vessels. *Cell 79*, 1157-64.

(158) Brakebusch, C., Bouvard, D., Stanchi, F., Sakai, T., and Fassler, R. (2002) Integrins in invasive growth. *J Clin Invest 109*, 999-1006.

(159) Keenan, R. M., Miller, W. H., Kwon, C., Ali, F. E., Callahan, J. F., Calvo, R. R., Hwang, S. M., Kopple, K. D., Peishoff, C. E., Samanen, J. M., Wong, A. S., Yuan, C. K., and Huffman, W. F. (1997) Discovery of potent nonpeptide vitronectin receptor (alpha v beta 3) antagonists. *J Med Chem 40*, 2289-92.

(160) Miller, W. H., Keenan, R. M., Willette, R. N., and Lark, M. W. (2000) Identification and in vivo efficacy of small-molecule antagonists of integrin alphavbeta3 (the vitronectin receptor). *Drug Discov Today 5*, 397-408.

(161) Pitts, W. J., Wityak, J., Smallheer, J. M., Tobin, A. E., Jetter, J. W., Buynitsky, J. S., Harlow, P. P., Solomon, K. A., Corjay, M. H., Mousa, S. A., Wexler, R. R., and Jadhav, P. K. (2000) Isoxazolines as potent antagonists of the integrin alpha(v)beta(3). *J Med Chem 43*, 27-40.

(162) Bogdanowich-Knipp, S. J., Chakrabarti, S., Williams, T. D., Dillman, R. K., and Siahaan, T. J. (1999) Solution stability of linear vs. cyclic RGD peptides. *J Pept Res 53*, 530-41.

(163) Bogdanowich-Knipp, S. J., Jois, D. S., and Siahaan, T. J. (1999) The effect of conformation on the solution stability of linear vs. cyclic RGD peptides. *J Pept Res 53*,

523-9.

(164) Bogdanowich-Knipp, S. J., Jois, S. D., and Siahaan, T. J. (1999) Effect of conformation on the conversion of cyclo-(1,7)-Gly-Arg-Gly-Asp-Ser-Pro-Asp-Gly-OH to its cyclic imide degradation product. *J Pept Res 54*, 43-53.

(165) Koivunen, E., Wang, B., and Ruoslahti, E. (1995) Phage libraries displaying cyclic peptides with different ring sizes: ligand specificities of the RGD-directed integrins. *Biotechnology (N Y) 13*, 265-70.

(166) Montet, X., Montet-Abou, K., Reynolds, F., Weissleder, R., and Josephson, L. (2006) Nanoparticle imaging of integrins on tumor cells. *Neoplasia 8*, 214-22.

(167) Zhang, C., Jugold, M., Woenne, E. C., Lammers, T., Morgenstern, B., Mueller, M. M., Zentgraf, H., Bock, M., Eisenhut, M., Semmler, W., and Kiessling, F. (2007) Specific targeting of tumor angiogenesis by RGD-conjugated ultrasmall superparamagnetic iron oxide particles using a clinical 1.5-T magnetic resonance scanner. *Cancer Res 67*, 1555-62.

(168) Pusztai, L., Mazouni, C., Anderson, K., Wu, Y., and Symmans, W. F. (2006) Molecular classification of breast cancer: limitations and potential. *Oncologist 11*, 868-77.

(169) Burstein, H. J. (2005) The distinctive nature of HER2-positive breast cancers. *N Engl J Med 353*, 1652-4.

(170) Burstein, H. J., and Winer, E. P. (2005) HER2 or not HER2: that is the question. *J Clin Oncol 23*, 3656-9.

(171) Peppercorn, J., Partridge, A., Burstein, H. J., and Winer, E. P. (2005) Standards for follow-up care of patents with breast cancer. *Breast 14*, 500-8.

(172) Engel, R. H., and Kaklamani, V. G. (2007) HER2-positive breast cancer: current and future treatment strategies. *Drugs 67*, 1329-41.

(173) Bartsch, R., Wenzel, C., Zielinski, C. C., and Steger, G. G. (2007) HER-2-positive breast cancer: hope beyond trastuzumab. *BioDrugs 21*, 69-77.

(174) Baselga, J., Perez, E. A., Pienkowski, T., and Bell, R. (2006) Adjuvant trastuzumab: a milestone in the treatment of HER-2-positive early breast cancer. *Oncologist 11 Suppl 1*, 4-12.

(175) Demonty, G., Bernard-Marty, C., Puglisi, F., Mancini, I., and Piccart, M. (2007) Progress and new standards of care in the management of HER-2 positive breast cancer. *Eur J Cancer 43*, 497-509.

(176) Jackisch, C. (2006) HER-2-positive metastatic breast cancer: optimizing trastuzumab-based therapy. *Oncologist 11 Suppl 1*, 34-41.

(177) Longo, R., Torino, F., and Gasparini, G. (2007) Targeted therapy of breast cancer. *Curr Pharm Des 13*, 497-517.

(178) Meric-Bernstam, F., and Hung, M. C. (2006) Advances in targeting human epidermal

growth factor receptor-2 signaling for cancer therapy. *Clin Cancer Res 12*, 6326-30.

(179) Ozols, R. F., Herbst, R. S., Colson, Y. L., Gralow, J., Bonner, J., Curran, W. J., Jr., Eisenberg, B. L., Ganz, P. A., Kramer, B. S., Kris, M. G., Markman, M., Mayer, R. J., Raghavan, D., Reaman, G. H., Sawaya, R., Schilsky, R. L., Schuchter, L. M., Sweetenham, J. W., Vahdat, L. T., and Winn, R. J. (2007) Clinical cancer advances 2006: major research advances in cancer treatment, prevention, and screening--a report from the American Society of Clinical Oncology. *J Clin Oncol 25*, 146-62.

(180) Mass, R. D. (2004) The HER receptor family: a rich target for therapeutic development. *Int J Radiat Oncol Biol Phys 58*, 932-40.

(181) Artemov, D., Mori, N., Okollie, B., and Bhujwalla, Z. M. (2003) MR molecular imaging of the Her-2/neu receptor in breast cancer cells using targeted iron oxide nanoparticles. *Magn Reson Med 49*, 403-8.

(182) Artemov, D., Mori, N., Ravi, R., and Bhujwalla, Z. M. (2003) Magnetic resonance molecular imaging of the HER-2/neu receptor. *Cancer Res 63*, 2723-7.

(183) Geninatti Crich, S., Cabella, C., Barge, A., Belfiore, S., Ghirelli, C., Lattuada, L., Lanzardo, S., Mortillaro, A., Tei, L., Visigalli, M., Forni, G., and Aime, S. (2006) In vitro and in vivo magnetic resonance detection of tumor cells by targeting glutamine transporters with Gd-based probes. *J Med Chem 49*, 4926-36.

(184) Goldenberg, D. M., and Nabi, H. A. (1999) Breast cancer imaging with radiolabeled antibodies. *Semin Nucl Med 29*, 41-8.

(185) Park, J. M., and Ikeda, D. M. (2006) Promising techniques for breast cancer detection, diagnosis, and staging using non-ionizing radiation imaging techniques. *Phys Med 21 Suppl 1*, 7-10.

(186) Persson, M., Tolmachev, V., Andersson, K., Gedda, L., Sandstrom, M., and Carlsson, J. (2005) [(177)Lu]pertuzumab: experimental studies on targeting of HER-2 positive tumour cells. *Eur J Nucl Med Mol Imaging 32*, 1457-62.

(187) Funovics, M. A., Kapeller, B., Hoeller, C., Su, H. S., Kunstfeld, R., Puig, S., and Macfelda, K. (2004) MR imaging of the her2/neu and 9.2.27 tumor antigens using immunospecific contrast agents. *Magn Reson Imaging 22*, 843-50.

(188) Ito, A., Kuga, Y., Honda, H., Kikkawa, H., Horiuchi, A., Watanabe, Y., and Kobayashi, T. (2004) Magnetite nanoparticle-loaded anti-HER2 immunoliposomes for combination of antibody therapy with hyperthermia. *Cancer Lett 212*, 167-75.

(189) Sakamoto, J. H., Smith, B. R., Xie, B., Rokhlin, S. I., Lee, S. C., and Ferrari, M. (2005) The molecular analysis of breast cancer utilizing targeted nanoparticle based ultrasound contrast agents. *Technol Cancer Res Treat 4*, 627-36.

(190) Lee, J. H., Huh, Y. M., Jun, Y. W., Seo, J. W., Jang, J. T., Song, H. T., Kim, S., Cho, E. J., Yoon, H. G., Suh, J. S., and Cheon, J. (2007) Artificially engineered magnetic nanoparticles for ultra-sensitive molecular imaging. *Nat Med 13*, 95-9.

(191) Jemal, A., Siegel, R., Ward, E., Murray, T., Xu, J., and Thun, M. J. (2007) Cancer

statistics, 2007. *CA Cancer J Clin 57*, 43-66.

(192) Mathers, C. D., and Loncar, D. (2006) Projections of global mortality and burden of disease from 2002 to 2030. *PLoS Med 3*, e442.

(193) Holcomb, S. S. (2007) Prostate cancer screening: an individual decision. *Nurse Pract 32*, 6-8.

(194) American Cancer Society. Cancer facts & figures 2007.

(195) Fuchsjager, M., Shukla-Dave, A., Akin, O., Barentsz, J., and Hricak, H. (2008) Prostate cancer imaging. *Acta Radiol 49*, 107-20.

(196) Hricak, H., Choyke, P. L., Eberhardt, S. C., Leibel, S. A., and Scardino, P. T. (2007) Imaging prostate cancer: a multidisciplinary perspective. *Radiology 243*, 28-53.

(197) Schiffer, E. (2007) Biomarkers for prostate cancer. *World J Urol 25*, 557-62.

(198) Taneja, S. S. (2004) Imaging in the diagnosis and management of prostate cancer. *Rev Urol 6*, 101-13.

(199) Karam, J. A., Mason, R. P., Koeneman, K. S., Antich, P. P., Benaim, E. A., and Hsieh, J. T. (2003) Molecular imaging in prostate cancer. *J Cell Biochem 90*, 473-83.

(200) Tricoli, J. V., Schoenfeldt, M., and Conley, B. A. (2004) Detection of Prostate Cancer and Predicting Progression: Current and Future Diagnostic Markers. *Clin Cancer Res 10*, 3943-3953.

(201) Beckett, M. L., Cazares, L. H., Vlahou, A., Schellhammer, P. F., and Wright, G. L., Jr. (1999) Prostate-specific Membrane Antigen Levels in Sera from Healthy Men and Patients with Benign Prostate Hyperplasia or Prostate Cancer. *Clin Cancer Res 5*, 4034-4040.

(202) Zhou, J., Scholes, J., and Hsieh, J. T. (2001) Signal transduction targets in androgen-independent prostate cancer. *Cancer Metastasis Rev 20*, 351-62.

(203) Chen, M. E., Lin, S. H., Chung, L. W., and Sikes, R. A. (1998) Isolation and characterization of PAGE-1 and GAGE-7. New genes expressed in the LNCaP prostate cancer progression model that share homology with melanoma-associated antigens. *J Biol Chem 273*, 17618-25.

(204) Lin, D. L., Tarnowski, C. P., Zhang, J., Dai, J., Rohn, E., Patel, A. H., Morris, M. D., and Keller, E. T. (2001) Bone metastatic LNCaP-derivative C4-2B prostate cancer cell line mineralizes in vitro. *Prostate 47*, 212-21.

(205) Liu, A. Y., Brubaker, K. D., Goo, Y. A., Quinn, J. E., Kral, S., Sorensen, C. M., Vessella, R. L., Belldegrun, A. S., and Hood, L. E. (2004) Lineage relationship between LNCaP and LNCaP-derived prostate cancer cell lines. *Prostate 60*, 98-108.

(206) Deshayes, S., Decaffmeyer, M., Brasseur, R., and Thomas, A. Structural polymorphism of two CPP: An important parameter of activity. *Biochimica et Biophysica Acta (BBA) - Biomembranes In Press, Uncorrected Proof*.

(207) Wadia, J. S., and Dowdy, S. F. (2005) Transmembrane delivery of protein and peptide drugs by TAT-mediated transduction in the treatment of cancer. *Adv Drug Deliv Rev 57*, 579-96.

(208) Zhou, J., Fan, J., and Hsieh, J. T. (2006) Inhibition of mitogen-elicited signal transduction and growth in prostate cancer with a small peptide derived from the functional domain of DOC-2/DAB2 delivered by a unique vehicle. *Cancer Res 66*, 8954-8.

(209) Futaki, S. (2006) Oligoarginine vectors for intracellular delivery: design and cellular-uptake mechanisms. *Biopolymers 84*, 241-9.

(210) Galustian, C., Foulds, S., Dye, J. F., and Guillou, P. J. (1994) Swainsonine, a glycosylation inhibitor, enhances both lymphocyte efficacy and tumour susceptibility in LAK and NK cytotoxicity. *Immunopharmacology 27*, 165-72.

(211) Wender, P. A., Mitchell, D. J., Pattabiraman, K., Pelkey, E. T., Steinman, L., and Rothbard, J. B. (2000) The design, synthesis, and evaluation of molecules that enable or enhance cellular uptake: peptoid molecular transporters. *Proc Natl Acad Sci U S A 97*, 13003-8.

(212) Muto, S., Sakuma, K., Taniguchi, A., and Matsumoto, K. (1999) Human mannose-binding lectin preferentially binds to human colon adenocarcinoma cell lines expressing high amount of Lewis A and Lewis B antigens. *Biol Pharm Bull 22*, 347-52.

(213) Richard, J. P., Melikov, K., Brooks, H., Prevot, P., Lebleu, B., and Chernomordik, L. V. (2005) Cellular uptake of unconjugated TAT peptide involves clathrin-dependent endocytosis and heparan sulfate receptors. *J Biol Chem 280*, 15300-6.

(214) Ferrari, A., Pellegrini, V., Arcangeli, C., Fittipaldi, A., Giacca, M., and Beltram, F. (2003) Caveolae-mediated internalization of extracellular HIV-1 tat fusion proteins visualized in real time. *Mol Ther 8*, 284-94.

(215) Fischer, R., Kohler, K., Fotin-Mleczek, M., and Brock, R. (2004) A stepwise dissection of the intracellular fate of cationic cell-penetrating peptides. *J Biol Chem 279*, 12625-35.

(216) Nakase, I., Tadokoro, A., Kawabata, N., Takeuchi, T., Katoh, H., Hiramoto, K., Negishi, M., Nomizu, M., Sugiura, Y., and Futaki, S. (2007) Interaction of arginine-rich peptides with membrane-associated proteoglycans is crucial for induction of actin organization and macropinocytosis. *Biochemistry 46*, 492-501.

(217) Console, S., Marty, C., Garcia-Echeverria, C., Schwendener, R., and Ballmer-Hofer, K. (2003) Antennapedia and HIV transactivator of transcription (TAT) "protein transduction domains" promote endocytosis of high molecular weight cargo upon binding to cell surface glycosaminoglycans. *J Biol Chem 278*, 35109-14.

(218) Medarova, Z., Pham, W., Farrar, C., Petkova, V., and Moore, A. (2007) In vivo imaging of siRNA delivery and silencing in tumors. *Nat Med 13*, 372-7.

(219) Anderson, C. J., Wadas, T. J., Wong, E. H., and Weisman, G. R. (2007) Cross-bridged macrocyclic chelators for stable complexation of copper radionuclides for positron emission tomography imaging. *Q J Nucl Med Mol Imaging*.

(220) Boswell, C. A., Sun, X. K., Niu, W. J., Weisman, G. R., Wong, E. H., Rheingold, A. L.,

and Anderson, C. J. (2004) Comparative in vivo stability of copper-64-labeled cross-bridged and conventional tetraazamacrocyclic complexes. *Journal Of Medicinal Chemistry 47*, 1465-1474.

(221) Sprague, J. E., Peng, Y., Fiamengo, A. L., Woodin, K. S., Southwick, E. A., Weisman, G. R., Wong, E. H., Golen, J. A., Rheingold, A. L., and Anderson, C. J. (2007) Synthesis, characterization and in vivo studies of Cu(II)-64-labeled cross-bridged tetraazamacrocycle-amide complexes as models of peptide conjugate imaging agents. *J Med Chem 50*, 2527-35.

(222) Groman, E. V., Bouchard, J. C., Reinhardt, C. P., and Vaccaro, D. E. (2007) Ultrasmall mixed ferrite colloids as multidimensional magnetic resonance imaging, cell labeling, and cell sorting agents. *Bioconjug Chem 18*, 1763-71.

(223) Lide, D. R. Hand book of chemistry and physics, 85 th Edition, 2004-2005, CRC Press.

(224) Hogemann, D., Ntziachristos, V., Josephson, L., and Weissleder, R. (2002) High throughput magnetic resonance imaging for evaluating targeted nanoparticle probes. *Bioconjug Chem 13*, 116-21.

(225) Liu, S., Wei, X., Chu, M., Peng, J., and Xu, Y. (2006) Synthesis and characterization of iron oxide/polymer composite nanoparticles with pendent functional groups. *Colloids Surf B Biointerfaces 51*, 101-6.

(226) Nitin, N., LaConte, L. E., Zurkiya, O., Hu, X., and Bao, G. (2004) Functionalization and peptide-based delivery of magnetic nanoparticles as an intracellular MRI contrast agent. *J Biol Inorg Chem 9*, 706-12.

(227) Hasegawa, M. e. a. Small-diameter composite composed of water-soluble carboxypolysaccharide and magnetic iron oxide. EP 0656368 A1 (1993).

(228) Analytical Chem., 25, 1656 (1953).

(229) Welling, P. G. Pharmacokinetics, American Chemical Society, Washington, DC., 1997. pp 271-296.

(230) Heymer, A., Haddad, D., Weber, M., Gbureck, U., Jakob, P. M., Eulert, J., and Noth, U. (2008) Iron oxide labelling of human mesenchymal stem cells in collagen hydrogels for articular cartilage repair. *Biomaterials 29*, 1473-83.

(231) Hahn, P., Milam, A. H., and Dunaief, J. L. (2003) Maculas affected by age-related macular degeneration contain increased chelatable iron in the retinal pigment epithelium and Bruch's membrane. *Arch Ophthalmol 121*, 1099-105.

(232) Stark, R. W. (2007) Atomic force microscopy: Getting a feeling for the nanoworld. *Nature Nanotechnology 2*, 461 - 462

(233) Sun, X., Kim, J., Martell, A. E., Welch, M. J., and Anderson, C. J. (2004) In vivo evaluation of copper-64-labeled monooxo-tetraazamacrocyclic ligands. *Nucl Med Biol 31*, 1051-9.

(234) Blower, P. J., Lewis, J. S., and Zweit, J. (1996) Copper radionuclides and

radiopharmaceuticals in nuclear medicine. *Nucl Med Biol 23*, 957-80.

(235) Wadas, T. J., Wong, E. H., Weisman, G. R., and Anderson, C. J. (2007) Copper chelation chemistry and its role in copper radiopharmaceuticals. *Curr Pharm Des 13*, 3-16.

(236) Moghimi, S. M., and Bonnemain, B. (1999) Subcutaneous and intravenous delivery of diagnostic agents to the lymphatic system: applications in lymphoscintigraphy and indirect lymphography. *Adv Drug Deliv Rev 37*, 295-312.

(237) Neuberger, T., Schopf, B., Hofmann, H., Hofmann, M., and von Rechenberg, B. (2005) Superparamagnetic nanoparticles for biomedical applications: Possibilities and limitations of a new drug delivery system. *Journal of Magnetism and Magnetic Materials 293*, 483-496.

(238) Rossin, R., Pan, D., Qi, K., Turner, J. L., Sun, X., Wooley, K. L., and Welch, M. J. (2005) 64Cu-labeled folate-conjugated shell cross-linked nanoparticles for tumor imaging and radiotherapy: synthesis, radiolabeling, and biologic evaluation. *J Nucl Med 46*, 1210-8.

(239) Kallrot, M., Edlund, U., and Albertsson, A. C. (2006) Surface functionalization of degradable polymers by covalent grafting. *Biomaterials 27*, 1788-96.

(240) Shenoy, D., Fu, W., Li, J., Crasto, C., Jones, G., DiMarzio, C., Sridhar, S., and Amiji, M. (2006) Surface functionalization of gold nanoparticles using hetero-bifunctional poly(ethylene glycol) spacer for intracellular tracking and delivery. *Int J Nanomedicine 1*, 51-7.

(241) Martina, M. S., Fortin, J. P., Menager, C., Clement, O., Barratt, G., Grabielle-Madelmont, C., Gazeau, F., Cabuil, V., and Lesieur, S. (2005) Generation of Superparamagnetic Liposomes Revealed as Highly Efficient MRI Contrast Agents for in Vivo Imaging. *J. Am. Chem. Soc. 127*, 10676-10685.